A&A 650, A205 (2021)
https://doi.org/10.1051/0004-6361/202140381

Astronomy & Astrophysics

A search for transiting planets around hot subdwarfs

I. Methods and performance tests on light curves from *Kepler*, K2, TESS, and CHEOPS⋆

V. Van Grootel[1], F. J. Pozuelos[1,2], A. Thuillier[1], S. Charpinet[3], L. Delrez[1,2,4], M. Beck[4], A. Fortier[5,6], S. Hoyer[7], S. G. Sousa[8], B. N. Barlow[9], N. Billot[4], M. Dévora-Pajares[10,11], R. H. Østensen[12], Y. Alibert[5], R. Alonso[13,14], G. Anglada Escudé[15,16], J. Asquier[17], D. Barrado[18], S. C. C. Barros[8,19], W. Baumjohann[20], T. Beck[5], A. Bekkelien[4], W. Benz[5,6], X. Bonfils[21], A. Brandeker[22], C. Broeg[5], G. Bruno[23], T. Bárczy[24], J. Cabrera[25], A. C. Cameron[26], S. Charnoz[27], M. B. Davies[28], M. Deleuil[7], O. D. S. Demangeon[8,19], B.-O. Demory[5], D. Ehrenreich[4], A. Erikson[25], L. Fossati[20], M. Fridlund[29,30], D. Futyan[4], D. Gandolfi[31], M. Gillon[2], M. Guedel[32], K. Heng[6,33], K. G. Isaak[17], L. Kiss[34,35,36], J. Laskar[37], A. Lecavelier des Etangs[38], M. Lendl[4], C. Lovis[4], D. Magrin[39], P. F. L. Maxted[40], M. Mecina[32,20], A. J. Mustill[28], V. Nascimbeni[39], G. Olofsson[22], R. Ottensamer[32], I. Pagano[23], E. Pallé[13,14], G. Peter[41], G. Piotto[42,39], J.-Y. Plesseria[43], D. Pollacco[33], D. Queloz[4,44], R. Ragazzoni[42,39], N. Rando[17], H. Rauer[25,45,46], I. Ribas[15,16], N. C. Santos[8,19], G. Scandariato[23], D. Ségransan[4], R. Silvotti[47], A. E. Simon[5], A. M. S. Smith[25], M. Steller[20], G. M. Szabó[48,49], N. Thomas[5], S. Udry[4], V. Viotto[39], N. A. Walton[50], K. Westerdorff[41], and T. G. Wilson[26]

(Affiliations can be found after the references)

Received 20 January 2021 / Accepted 14 April 2021

ABSTRACT

Context. Hot subdwarfs experienced strong mass loss on the red giant branch (RGB) and are now hot and small He-burning objects. These stars constitute excellent opportunities for addressing the question of the evolution of exoplanetary systems directly after the RGB phase of evolution.

Aims. In this project we aim to perform a transit survey in all available light curves of hot subdwarfs from space-based telescopes (*Kepler*, K2, TESS, and CHEOPS) with our custom-made pipeline `SHERLOCK` in order to determine the occurrence rate of planets around these stars as a function of orbital period and planetary radius. We also aim to determine whether planets that were previously engulfed in the envelope of their red giant host star can survive, even partially, as a planetary remnant.

Methods. For this first paper, we performed injection-and-recovery tests of synthetic transits for a selection of representative *Kepler*, K2, and TESS light curves to determine which transiting bodies in terms of object radius and orbital period we will be able to detect with our tools. We also provide estimates for CHEOPS data, which we analyzed with the `pycheops` package.

Results. Transiting objects with a radius $\lesssim$1.0 $R_\oplus$ can be detected in most of the *Kepler*, K2, and CHEOPS targets for the shortest orbital periods (1 d and shorter), reaching values as low as ∼0.3 $R_\oplus$ in the best cases. Sub-Earth-sized bodies are only reached for the brightest TESS targets and for those that were observed in a significant number of sectors. We also give a series of representative results for larger planets at greater distances, which strongly depend on the target magnitude and on the length and quality of the data.

Conclusions. The TESS sample will provide the most important statistics for the global aim of measuring the planet occurrence rate around hot subdwarfs. The *Kepler*, K2, and CHEOPS data will allow us to search for planetary remnants, that is, very close and small (possibly disintegrating) objects.

Key words. planet-star interactions – planetary systems – stars: horizontal-branch – subdwarfs – techniques: photometric

1. Introduction

Hot subdwarf B (sdB) stars are hot and compact stars ($T_{\rm eff}$ = 20 000–40 000 K and log g = 5.2–6.2; Saffer et al. 1994) that lie on the blue tail of the horizontal branch (HB), that is, the extreme horizontal branch (EHB). The HB stage corresponds to core-He burning objects and follows the red giant branch (RGB) phase. Unlike most post-RGB stars that cluster at the red end of the HB (the so-called red clump, RC) because they lose almost no envelope on the RGB (Miglio et al. 2012), sdB stars experienced strong mass loss on the RGB and have extremely thin residual H envelopes ($M_{\rm env}$ < 0.01 $M_\odot$, Heber 1986). This extremely thin envelope explains their high effective temperatures and their inability to sustain H-shell burning. This prevents these stars from ascending the asymptotic giant branch (AGB) after core-He exhaustion (Dorman et al. 1993). About 60% of the sdBs reside in binary systems, and about half of them are in close binaries with orbital periods of up to a few days (see, e.g., Allard et al. 1994;

⋆ CHEOPS data presented in Fig. 5 and lists presented in Appendices C and D are only available at the CDS via anonymous ftp to `cdsarc.u-strasbg.fr` (`130.79.128.5`) or via `http://cdsarc.u-strasbg.fr/viz-bin/cat/J/A+A/650/A205`

Maxted et al. 2001), while the other half resides in wider binaries with orbital periods of up to several years (Stark & Wade 2003; Vos et al. 2018). Binary interactions (through common-envelope, CE, evolution for the short orbits, and stable Roche-lobe overflow, RLOF, evolution for the wide orbits) are therefore the main reasons for this extreme mass loss (Han et al. 2002, 2003). The hot O-type subdwarfs, or sdO stars, have $T_{\rm eff}$ = 40 000–80 000 K and a wide range of surface gravities. The compact sdO stars ($\log g = 5.2-6.2$) are either post-EHB objects or direct post-RGB objects (through a so-called late hot He-flash; Miller Bertolami et al. 2008), or end products of merger events (Iben 1990; Saio & Jeffery 2000, 2002). The sdOs with $\log g < 5.2$ are post-AGB stars, that is, stars that have ascended the giant branch a second time after core-He burning exhaustion (Reindl et al. 2016).

The formation of the approximately 40% of sdB stars that appear to be single has been a mystery for decades. In the absence of a companion, it is hard to explain how the star can expel most of its envelope on the RGB and still achieve core-He burning ignition. Recently, Pelisoli et al. (2020) suggested that all sdB stars might originate from binary evolution. Merger scenarios involving two low-mass white dwarfs have also been investigated (Webbink 1984; Han et al. 2002, 2003; Zhang & Jeffery 2012), but several facts challenge this hypothesis. First, compact low-mass white dwarf binaries are quite rare, even though some candidates are identified (Ratzloff et al. 2019). Second, the mass distributions of single and binary sdB stars are indistinguishable (Fontaine et al. 2012, Table 3 in particular). This mass distribution is mainly obtained from asteroseismology (some sdB stars exhibit oscillations, which allow the precise and accurate determination of the stellar parameters, including total mass; Van Grootel et al. 2013) and also from binary light-curve modeling for hot subdwarfs in eclipsing binary systems. Single and binary mass distributions peak at $\sim$0.47 $M_\odot$, which is the minimum core mass required to ignite He through a He-flash at the tip of RGB (stars of $\gtrsim$2.3 $M_\odot$ are able to ignite He quietly at lower core masses, down to $\sim$0.33 $M_\odot$, but the more massive the stars, the rarer they are). A mass distribution of single sdB stars from mergers, in contrast, would be much broader (0.4–0.7 $M_\odot$; Han et al. 2002). With the DR2 release of *Gaia* (Gaia Collaboration 2018) and precise distances for many hot subdwarfs (Geier 2020), it is now also possible to build a spectrophotometric mass distribution for a much larger sample than what was achieved with the hot subdwarf pulsators or those in eclipsing binaries. Individual masses are much less precise than those obtained by asteroseismology or binary light-curve modeling (Schneider et al. 2019). However, single and binary spectrophotometric mass distributions share the same properties here as well, which tends to disprove the hypothesis of different origins for single and binary sdB stars. The third piece of evidence against merger scenarios (which would most likely result in fast-rotating objects) is the very slow rotation of almost all single sdB stars, as obtained through $v \sin i$ measurements (Geier & Heber 2012) or from asteroseismology (Charpinet et al. 2018). Moreover, their rotation rates are in direct line with the core rotation rates observed in RC stars (Mosser et al. 2012), which is another strong indication that these stars and the single sdB stars do share a same origin, that is, that they are post-RGB stars.

The question of the evolution of exoplanet systems after the main sequence of their host is generally addressed by studying exoplanets around subgiants, RGB stars, and normal HB (RC) stars (hereafter the 'classical' evolved stars). These classical evolved stars are typically very large stars, with radii ranging from $\sim$5–10 $R_\odot$ to more than 1000 $R_\odot$. This is much larger than hot subdwarfs, which have radii in the range $\sim$0.1–0.3 $R_\odot$ (Heber 2016). Their mass is typically higher than $\sim$1.5 $M_\odot$, compared to $\sim$0.47 $M_\odot$ for hot subdwarfs. The transit and radial velocity (RV) methods are both challenging for these classical evolved stars because the transit depth is diluted and there are additional noise sources (Van Eylen et al. 2016). Another difficulty for the question of the fate of exoplanet systems after the RGB phase itself is the difficulty of distinguishing RGB and RC stars based on their spectroscopic parameters alone, which is sometimes hard even with help of asteroseismology (Campante et al. 2019). As a consequence, only large or massive planets are detected around the classical evolved stars (Jones et al. 2021, and references therein). A dearth of close-in giant planets is observed around these evolved stars compared to solar-type main-sequence stars (Sato et al. 2008; Döllinger et al. 2009). This may be caused by planet engulfment by the host star, but current technologies do not allow us to determine whether smaller planets and remnants (such as the dense cores of former giant planets) are present. The lack of close-in giant planets may also be explained by the intrinsically different planetary formation for these intermediate-mass stars (see the discussion in Jones et al. 2021). Ultimately, the very existence of planet remnants may be linked to the ejection of most of the envelope on the RGB that occurs for hot subdwarfs, while for classical evolved stars, nothing stops the in-spiraling planet inside the host star, and in all cases, the planet finally merges with the star, is fully tidally disrupted, or is totally ablated by heating or by the strong stellar wind. In other words, the ejection of the envelope not only enables the detection of small objects as remnants, but most importantly, it may even be the reason for the existence of these remnants by stopping the spiraling-in in the host star.

Many studies have focused on white dwarfs (the ultimate fate of $\sim$97% of all stars), including the direct observations of transiting disintegrating planetesimals (Vanderburg et al. 2015), the accretion of a giant planet (Gänsicke et al. 2019), and, most recently, the transit of a giant planet (Vanderburg et al. 2020). More than 25% of all single white dwarfs exhibit metal pollution in their atmospheres (which should be pure H or He because of the gravitational settling of heavier elements in these objects with very high surface gravities), which is generally interpreted as material accretion of surrounding planetary remnants (Hollands et al. 2018, and references therein). Statistics on the occurrence rate of planets around white dwarfs as a function of orbital period and planet radius have also been established (Fulton et al. 2014; van Sluijs & Van Eylen 2018; Wilson et al. 2019). However, the vast majority of white dwarfs experienced two giant phases of evolution, namely the RGB and the AGB. The AGB expansion and strong mass loss, followed by the planetary-nebula phase, will have a profound effect on the orbital stability of the surrounding bodies (e.g., Debes & Sigurdsson 2002; Mustill et al. 2014; Maldonado et al. 2021). Hence no direct conclusion concerning the effect of RGB expansion alone on the exoplanet systems can be drawn from white dwarfs.

Hot subdwarfs therefore constitute excellent opportunities for addressing the question of the evolution of exoplanet systems after the RGB phase of evolution. It is precisely this potential we aim to exploit in this project by determining the occurrence rate of planets around hot subdwarfs as a function of orbital period and planet radius. We achieve this objective by performing a transit search in all available light curves of hot subdwarfs from space-based observatories, such as *Kepler* (Borucki et al. 2010), K2 (Howell et al. 2014), TESS (Ricker et al. 2014), and CHEOPS

(Benz et al. 2021). In this first paper, we provide a review of the current status of the search of planets around hot subdwarfs with the different detection methods in Sect. 2. We present the observations and the tools we used to perform our transit search in Sect. 3. We provide extensive tests of the photometric quality of the light curves in Sects. 4 and 5, and we conclude and outline future work in Sect. 6.

2. Search for planets around hot subdwarfs: current status

To date, several planet detections around hot subdwarfs have been claimed, but none of them received confirmation. With the pulsation-timing method (variation in the oscillation periods of sdB pulsators), planets of a few Jupiter masses in orbits at about 1 AU were announced around V391 Peg and DW Lyn (Silvotti et al. 2007; Lutz et al. 2012), but these claims have recently been refuted (Silvotti et al. 2018; Mackebrandt et al. 2020). Based on weak signals that were interpreted as reflection and thermal re-emission in *Kepler* light curves, five very close-in (with orbital periods of a few hours) Earth-sized planets have been claimed to orbit KIC 05807616 (Charpinet et al. 2011) and KIC 10001893 (Silvotti et al. 2014). However, the attribution of these signals to exoplanets is debatable (Krzesinski 2015; Blokesz et al. 2019). Using the RV method, Geier et al. (2009) announced the discovery of a close-in ($P_{\rm orb} = 2.4$ days) planet of several Jupiter masses around HD 149382, but this was ruled out by high-precision RV measurements obtained with the *Hobby-Eberly* Telescope spectrograph, which excluded the presence of almost any substellar companion with $P_{\rm orb} < 28$ days and $M \sin i \gtrsim 1 M_{\rm Jup}$ (Norris et al. 2011). No close massive planets (down to a few Jupiter masses) were found from a mini RV survey carried out with the HARPS-N spectrograph on eight apparently single hot subdwarfs (Silvotti et al. 2020).

Several ground-based surveys with both photometric and RV techniques target the red dwarf or brown dwarf close companions to hot subdwarfs (Schaffenroth et al. 2018, 2019). These companions are frequent (Schaffenroth et al. 2018), but no Jupiter-like planets have been found to date. In contrast, several discoveries of circumbinary massive planets have been announced in close, post-CE evolution sdB+dM eclipsing systems through eclipse-timing variations, for instance, HW Vir, the prototype of the class (Lee et al. 2009; Beuermann et al. 2012), NSVS 14256825 (Zhu et al. 2019), HS 0705+6700 (Pulley et al. 2015), NY Vir (Qian et al. 2012), and 2M 1938+4603 (Baran et al. 2015). These planets might correspond to first-generation, second-generation (Schleicher & Dreizler 2014; Völschow et al. 2014), or hybrid planets (which are formed from ejected stellar material that is accreted onto remnants of first-generation planets; Zorotovic & Schreiber 2013). All but one of the ten well-studied HW Vir systems show eclipse-timing variations (Heber 2016; Marsh 2018). This may call for another explanation than planets (perhaps something analogously to the mechanism suggested for eclipse-timing variations in white dwarf binaries; Bours et al. 2016) because the occurrence of circumbinary planets around close main-sequence binaries that are the progenitors of such systems is only ∼1% (Welsh et al. 2012). The properties of the claimed planets often change or are discarded after new measurements (Heber 2016; Marsh 2018), while the orbits are regularly found to be dynamically unstable (e.g., Wittenmyer et al. 2013). None of these claimed circumbinary planets has been confirmed through another technique.

3. Observations and methods

3.1. Space-based light curves of hot subdwarfs

In the original *Kepler* field, 72 hot subdwarfs were observed at the short cadence (SC) of 1 min for at least one quarter, including the commissioning quarter Q0, which started on 2 May 2009. During the one-year survey phase that followed Q0 (quarters Q1 of 33.5 days and Q2 to Q4 of 90 days each, divided into monthly subquarters), 15 sdB stars were found to pulsate (Østensen et al. 2010, 2011). These 15 stars were consequently observed for the rest of the mission at SC (with exceptions of some quarters for some sdB pulsators, see the details in Table A.1). Three other sdB pulsators, known as B3, B4, and B5, were found in the open cluster NGC 6791 (Pablo et al. 2011) and were observed at SC for various durations (see Table A.1). Of the non-pulsators, 47 B-type hot subdwarfs (sdB and sdOB) were observed for at least one month at SC (5 of them for several quarters), as well as 7 sdO stars. At the long cadence (LC) of 30 min, these 54 non-pulsating hot subdwarfs were generally observed for several quarters, and some of them for the whole duration of the mission. The list of hot subdwarf targets in the original *Kepler* field and details on the observing quarters in SC and LC can be found in Table A.1. The primary *Kepler* mission stopped on 11 May 2013, during Q17.2, after the failure of a second reaction wheel that was necessary to stabilize the spacecraft and obtain the fine and stable pointing for observations of the original field.

The *Kepler* mission was then redesigned as K2, for which the two remaining reaction wheels allowed a stable pointing for ∼80 days of fields close to the ecliptic. An engineering test of 11 days in February 2014 confirmed the feasibility of this strategy, and 19 campaigns (campaign 0–18) were executed from March 2014 to July 2018, when exhaustion of propellants definitively ended the mission. When we account only for confirmed hot subdwarfs, 39 sdB/sdOB pulsators were observed at SC through at least one campaign in K2 fields. Two more sdB pulsators were discovered through LC data only. Seventy-nine more sdB/sdOB non-pulsators and 10 sdO non-pulsators were also observed at SC. Finally, 44 hot subdwarfs were observed at LC only. In contrast to *Kepler*, the K2 SC and LC data generally cover only one campaign (of about 80 days duration), although a few stars were observed in two or three campaigns. The full list of hot subdwarfs observed by K2 and details can be found in Table B.1.

TESS (Transiting Exoplanet Survey Satellite) has been operational since July 2018. It is performing a high-precision photometric survey over almost the whole sky (about 90%), avoiding only a narrow band around the ecliptic[1]. The TESS primary two-year mission, which ended in early July 2020, consisted of 26 sectors that were observed nearly continuously for ∼27.4 days each. Some overlap between sectors exists for the highest northern and southern ecliptic latitudes, therefore some stars have been observed for several sectors (see Table 1). The primary mission TESS data products consist of SC observations sampled every 2 min for selected stars, as well as full-frame images (FFI) taken every 30 min that contain data for all stars in the field of view. Accounting for confirmed hot subdwarfs alone, 1302 stars were observed for at least one sector at SC during primary mission. This list was assembled by Working Group (WG) 8 on compact pulsators of the TESS Asteroseismic Consortium (TASC; see also Stassun et al. 2019). Table 1 presents the statistics for these TESS primary mission observations of hot subdwarfs, and the full list can be found online[2] (see Appendix C

[1] https://tess.mit.edu/observations/
[2] https://github.com/franpoz/Hot-Subdwarfs-Catalogues

Table 1. Statistics for the hot subdwarfs observed in the primary TESS mission (July 2018–July 2020).

Number of sectors	Number of stars
1	877
2	205
3	72
4	23
5	21
6	24
7	7
8	10
9	6
10	6
11	13
12	23
13	15
G magnitude	Number of stars
8–9	3
9–10	4
10–11	18
11–12	60
12–13	162
13–14	278
14–15	384
15–16	341
16–17	51
Beyond 17	1

for details). The TESS extended mission started on 4 July 2020, and revisits all sectors for the same duration. The sectors are referred to with increasing numbers (Sector 27, 28, etc.). An 'ultra short cadence' of 20 s is now available in addition to the normal SC of 2 min, and FFIs are now taken every 10 min. After release of Sectors 27–31, 243 confirmed hot subdwarfs have been observed at 20 s cadence, and 670 more at a 2-min cadence (these targets were also selected by WG8 of the TASC). Most of these targets were previously observed in the primary mission (sectors 1–26), but about one-third are new targets that were not observed during the primary mission[3] (see Appendix D for details). It is expected that about 2300 hot subdwarfs will have been observed at the end of the two-year extended mission.

CHEOPS (CHaracterising ExOPlanets Satellite) is a European Space Agency (ESA) mission primarily dedicated to the study of known extrasolar planets orbiting bright ($6 < V < 12$) stars. It was successfully launched into a 700 km altitude Sun-synchronous 99-min orbit on 18 December 2019. CHEOPS is a 30 cm (effective) aperture telescope optimized for obtaining high-cadence high-precision photometric observations for one single star at a time in a broad optical band. CHEOPS is a pointed mission with mostly time-critical observations, therefore it has ~20% of free orbits that are partly used to observe bright apparently single hot subdwarfs as a "filler" program (program ID002). This means that hot subdwarf observations are carried out when CHEOPS has no time-constrained or higher-priority observations. The selected targets are generally close to the ecliptic where CHEOPS has its maximum visibility (but they were not observed by K2) and are observed for one to three consecutive orbits with the goal of a total of 18 orbits per target per season. As of 19 December 2020 (eight months after starting the program), 46 hot subdwarf targets have been observed by CHEOPS for a total of 290 orbits. The exposure time is 60 sec for all these targets (except for HD 149382, for which it is 41 s). The list of CHEOPS targets and details can be found in Table 2 (the columns "Phase coverage" and "Minimum planet size" are explained in Sect. 5), and online[4]. The nominal duration of the CHEOPS mission is 3.5 yr (i.e., until the end of 2023), when we hope to reach a total of about 25–30 orbits on 50–60 targets.

Finally, for completeness, we mention that the CoRoT satellite (Baglin et al. 2006) performed for ~24 days a high-quality, nearly continuous photometric observation of the sdB pulsator KPD 0629-0016 (Charpinet et al. 2010). We will add these observations in our transit survey, but we did not carry out a performance test for this one star here.

Figure 1 (top) summarizes the available sample of hot subdwarf space-based light curves ranked per bin of *G* magnitudes, as obtained from *Kepler*, K2, TESS (primary mission, as well as hot subdwarfs observed for the first time in the extended mission), and CHEOPS (as of 19 December 2020). No *G* magnitude is available for a few *Kepler* and K2 targets, therefore they are included in Fig. 1 with Kp minus 0.1, which is the mean difference between Kp and *G* magnitudes observed for targets for which both estimates are available. Figure 1 (bottom) shows the celestial distribution of this sample.

3.2. Tools for transit searches in space-based light curves

To search for transit events, we will make use of our custom pipeline SHERLOCK (Pozuelos et al. 2020)[5]. This pipeline provides the user with easy access to *Kepler*, K2, and TESS data for both SC and LC. The pipeline searches for and downloads the pre-search data conditioning simple aperture (PDC-SAP) flux data from the NASA Mikulski Archive for Space Telescope (MAST). Then, it uses a multi-detrend approach in the WOTAN package (Hippke et al. 2019), whereby the nominal PDC-SAP flux light curve is detrended several times using a biweight filter or a Gaussian process, by varying the window size or the kernel size, respectively. This multi-detrend approach is motivated by the associated risk of removing transit signals, in particular, short and shallow signals. Each of the new detrended light curves, jointly with the nominal PDC-SAP flux, is then processed through the TRANSIT LEAST SQUARES (TLS) package (Hippke & Heller 2019) in the search for transits. In contrast to the classical box least-squares (BLS) algorithm (Kovács et al. 2002), the TLS algorithm uses an analytical transit model that takes the stellar parameters into account. Then, it phase folds the light curves over a range of trial periods (P), transit epochs (T_0), and transit durations (d). It then computes the χ^2 between the model and the observed values, searching for the minimum χ^2 value in the 3D parameter space (P, T_0 , and d). The TLS algorithm has been found to be more reliable than the classical BLS in finding any type of transiting planet, and it is particularly well suited for the detection of small planets in long time series, such as those coming from *Kepler*, K2, and TESS. The TLS algorithm also allows the user to easily fine-tune the parameters to optimize the search in each case, which is particularly interesting

[3] The list can be found at https://github.com/franpoz/Hot-Subdwarfs-Catalogues

[4] https://github.com/franpoz/Hot-Subdwarfs-Catalogues

[5] The SHERLOCK code (Searching for Hints of Exoplanets from Lightcurves of space-based seekers) is fully available at the GitHub site https://github.com/franpoz/SHERLOCK

Table 2. Hot subdwarf targets observed by CHEOPS (as of 19 December 2020).

Name	Type	G mag	# of orbits (as of 19 Nov. 2020)	Phase coverage (days, for >80% coverage)	Min. planet size ($R_\oplus$, for $S/N = 5$ and 0.18 $R_\odot$ host)
Active					
HD 149382	sdB	8.80	14 (7 × 2)	0.47	0.4
HD 127493	sdO	9.96	6.8 (2 × 1 + 4.8)	0.18	0.4
TYC 981-1097-1	sd	12.01	18 (6 × 3)	0.68	0.7
Feige 110	sdOB	11.79	6 (3 × 2)	0.25	0.7
CW83-1419-09	sdOB	12.04	12 (4 × 3)	0.39	0.7
EC 14248-2647	sdOB	11.98	2 (1 × 2)	<0.10	0.7
PG 2219+094	sdB	11.90	5 (5 × 1)	0.18	0.7
PG 1352-023	sdOB	12.06	6 (3 × 2)	0.18	0.8
LS IV -12 1	sdO	11.11	4 (4 × 1)	0.18	0.8
Feige 14	sdB	12.77	5 (5 × 1)	0.11	0.8
EC 22081-1916	sdB	12.94	6 (3 × 2)	0.25	0.8
LS IV+06 2	He-sdO	12.14	5 (5 × 1)	0.18	0.8
MCT 2350-3026	sdO	12.07	8 (4 × 2)	0.32	0.8
TYC 982-614-1	sd	12.21	18 (6 × 3)	0.68	0.8
EC 20305-1417	sdB	12.34	6 (2 × 3)	0.25	0.8
LS IV+109	He-sdO	11.97	10 (5 × 2)	0.39	0.8
PG 1432+004	sdB	12.75	4 (2 × 2)	0.11	0.8
TonS403	sdO	12.92	11 (11 × 1)	0.25	0.8
TYC 497-63-1	sdB	12.89	5 (5 × 1)	0.11	0.8
TYC 999-2458-1	sdB	12.59	3 (1 × 3)	0.18	0.9
TYC 499-2297-1	sdB	12.63	12 (6 × 2)	0.54	0.9
LS IV+00 21	sdOB	12.41	4 (2 × 2)	0.18	0.9
PG 1245-042	sd	13.60	7 (7 × 1)	0.18	1.0
PG 2151+100	sdB	12.68	9 (3 × 3)	0.39	1.0
EC 13047-3049	sdB	12.78	2 (1 × 2)	<0.10	1.0
PG 1505+074	sdB	12.37	2 (2 × 1)	<0.10	1.0
LS IV -14 116	He-sdOB	12.98	2 (2 × 1)	0.11	1.0
EC 12578-2107	sdB	13.52	7 (7 × 1)	0.25	1.0
EC 13080-1508	sdB	13.65	3 (3 × 1)	0.18	1.0
PB 8783	sdO+F	12.23	6 (3 × 2)	0.25	1.1
MCT 2341-3443	sdB	10.92	4 (2 × 2)	0.18	1.1
EC 21595-1747	sdOB	12.62	4 (2 × 2)	0.18	1.1
PG 1230+067	He-sdOB	13.12	2 (1 × 2)	0.11	1.1
EC 15103-1557	sdB	12.82	6 (3 × 2)	0.25	1.1
PG 2313-021	sdB	13.00	6 (3 × 2)	0.18	1.1
PG 2349+002	sdB	13.27	10 (1 × 10)	0.32	1.1
PG 1207-033	sdB	13.34	2 (2 × 1)	0.11	1.1
PG 1303-114	sdB	13.63	5 (5 × 1)	0.18	1.1
PG 1343-102	sdB	13.69	4 (4 × 1)	0.25	1.1
Suspended					
LS IV+06 5	sdB	12.37	8 (4 × 2)	–	>1.3
EC 14338-1445	sdB	13.55	2 (2 × 1)	–	>1.5
EC 14599-2047	sdB	13.57	3 (3 × 1)	–	>1.5
EC 01541-1409	sdB	12.27	12 (4 × 3)	–	>1.5
TYC 1077-218-1	sdOB	12.41	3 (3 × 1)	–	>2.0
LS IV +09 2	sdB	12.69	4 (2 × 2)	–	>2.0
TYC 467-3836-1	sdB	11.70	6 (6 × 1)	–	>2.0

for shallow transits. In addition, SHERLOCK incorporates a vetting module that combines the `TPFplotter` (Aller et al. 2020), `LATTE` (Eisner et al. 2020), and `TRICERATOPS` (Giacalone et al. 2021) packages, which allows the user to explore any contamination source in the photometric aperture used, momentum dumps, background flux variations, x–y centroid positions, aperture size dependences, flux in-and-out transits, each individual pixel of the target pixel file, and to estimate the probabilities for different astrophysical scenarios such as transiting planet, eclipsing binary, and eclipsing binary with twice the orbital period. Collectively, these analyses help the user estimate the reliability of a given detection.

For each event that passes the vetting process, the user may wish to perform ground- or space-based follow-up observations to confirm the transit event on the target star. This is particularly critical for TESS observations because of the large pixel size (21 arcsec) and point spread function (which can be as large as 1 arcmin). These aspects increase the probability of

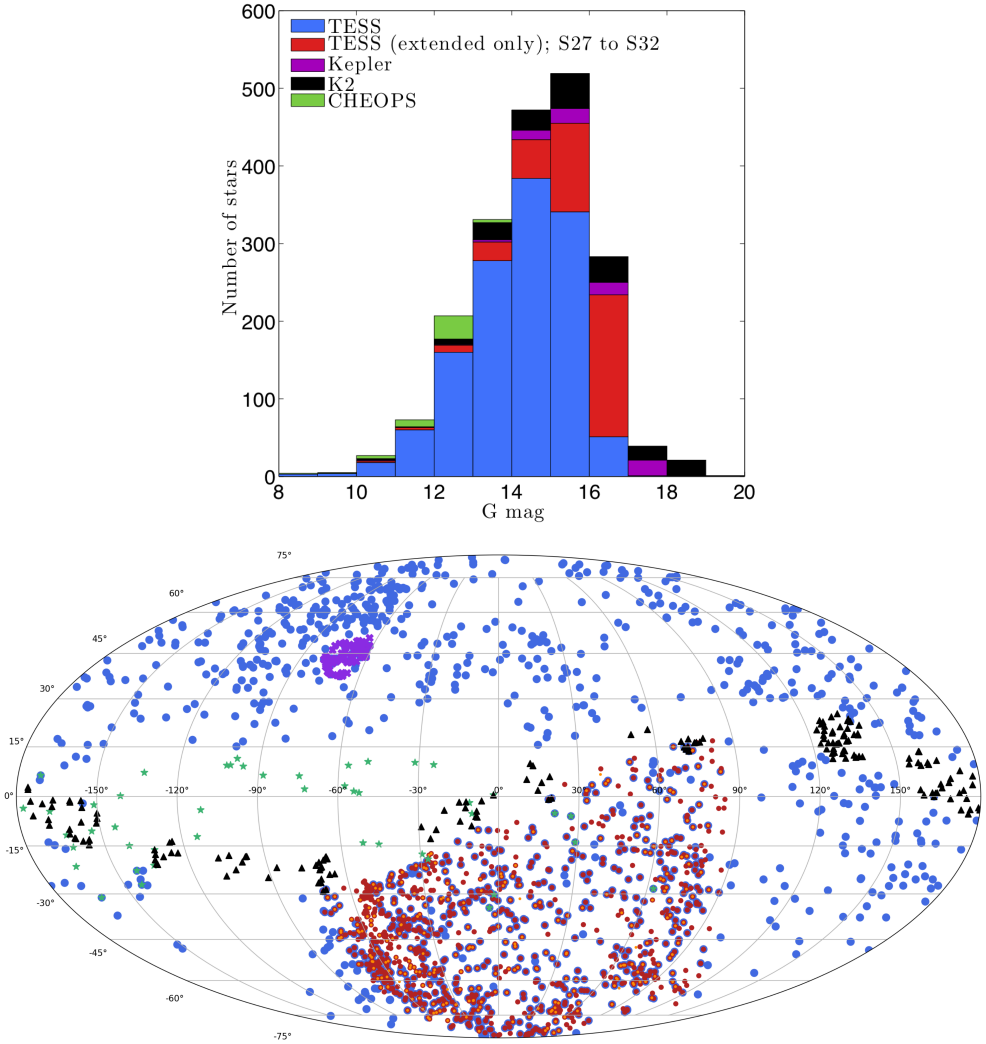

Fig. 1. *Top*: number of hot subdwarfs per *G*-magnitude bin observed by *Kepler*, K2, TESS (hot subdwarfs observed in primary mission, which are almost all reobserved in the extended mission), TESS extended only (hot subdwarfs observed for the first time in the extended mission; S27 to S32), and CHEOPS (as of 19 December 2020). *Bottom*: celestial distribution of these hot subdwarfs: TESS primary mission (blue dots), TESS extended mission 2 min and 20 s (red and dark orange dots), *Kepler* (purple crosses), K2 (black triangles), and CHEOPS (green stars).

contamination by a nearby eclipsing binary (see, e.g., Günther et al. 2019; Kostov et al. 2019; Quinn et al. 2019; Nowak et al. 2020). However, the results coming directly from the searches performed with SHERLOCK through the TLS algorithm are not optimal; that is, the associated uncertainties of P, T_0, and d are large, and their temporal propagation makes using them to compute future observational windows and to schedule a follow-up campaign impractical. SHERLOCK therefore uses the results coming from TLS as priors to perform model fitting, injecting them into `allesfitter` (Günther & Daylan 2019, 2021). The user can then choose between nested sampling or a Markov chain Monte Carlo (MCMC) analysis, whose posterior distributions are much more refined, with significant reductions of a few orders of magnitude of the uncertainties of P, T_0, and d. This allows us to schedule a follow-up campaign for which the observational windows are more reliable.

4. Injection-and-recovery tests

To quantify the detectability of transiting bodies in our sample of hot subdwarfs, we performed a suite of injection-and-recovery tests. While the detectability of a transit depends on the target and on the sector or quarter, these experiments allowed us to verify the general reliability of our survey. We explored several data sets coming from the *Kepler*, K2, and TESS missions. For each one, we chose a range of stellar magnitudes that we studied. In all cases, we followed the procedure described by Pozuelos et al. (2020) and Demory et al. (2020); that is, we downloaded the PDC-SAP fluxes in each case and generated a grid of synthetic transiting planets by varying their orbital periods and radii, which were injected in the downloaded light curves. We then detrended the light curves and searched for the injected planets. The search itself was done by applying the simple TLS algorithm. The multi-detrend approach applied by SHERLOCK makes it more efficient at finding shallow-periodic transits, but with a higher computational cost. The full use of SHERLOCK in the injection-and-recovery experiments is therefore too expensive. This means that our findings in these experiments might be considered as upper limits for the minimum planet sizes, and during our survey, we might detect even smaller planets. We defined a synthetic planet as "recovered" when we detect its epoch with a one-hour accuracy and if we find its period with an accuracy better than 5%. Depending on the number of available sectors or quarters, we explored the $R_{\rm planet}$–$P_{\rm planet}$ parameter space in different ranges. We conducted two different experiments to qualify the performances that can be achieved with *Kepler*, K2, and TESS data. The first experiment consisted of full injection-and-recovery tests focusing on a region of the parameter space corresponding to small close-in exoplanets. For *Kepler* and K2, the injected planet range was 0.3–1.0 $R_\oplus$ with steps of 0.1 $R_\oplus$, and 0.5–4.1 d with steps of 0.2 d for a total of 152 scenarios. For TESS, the injected planets have 0.5–3.0 $R_\oplus$ with steps of

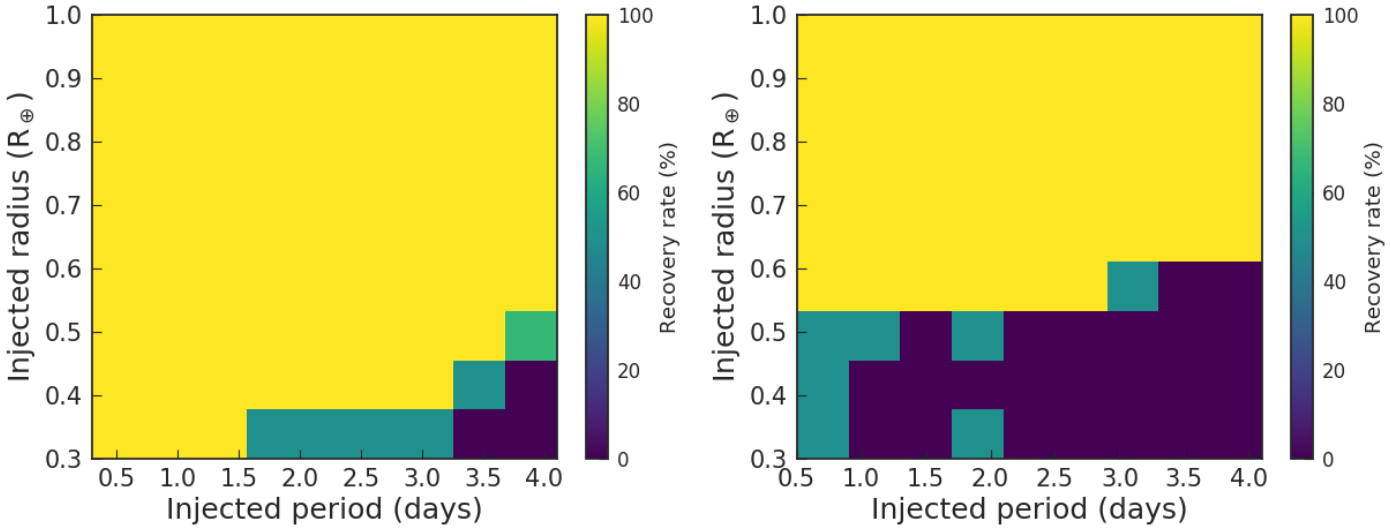

Fig. 2. Injection-and-recovery tests. *Left panel*: KIC 8054179 (Kp = 14.40, $G = 14.34$), based on Q6 *Kepler* data (90 days). *Right panel*: EPIC 206535752 (Kp = 13.99, $G = 14.10$), observed during Campaign 3 of K2 (81 days). Injected transits of planets have 0.3–1.0 $R_\oplus$ (steps of 0.1 $R_\oplus$) with 0.5–4.1 d (steps of 0.2 d) orbital periods.

0.05 $R_\oplus$, and 1.0–6.0 d with steps of 0.1 d, that is, a total of 2500 scenarios for each of them. However the six-sector test was made with 0.5–2.5 $R_\oplus$ with steps of 0.2 $R_\oplus$, and 1.0–5.0 d with steps of 0.2 d, for a total of 200 scenarios for computer-cost reasons (as a corollary, injection-and-recovery tests on more sectors, up to 13 sectors for one-year-continuous observations, are beyond our reach). The second experiment concerned larger planets at greater distances, that is, up to 10.0 $R_\oplus$ and 35 d orbital period. Full injection-and-recovery tests with sufficiently small steps led to a too high computational cost. We instead chose to focus on particular periods (1, 5, 15, 25, and 35 d) and determined the minimum planet size detectable for each set of data considered for these periods. This limit of 35 d is justified by the transit probability, which quickly decreases to very low values with increasing orbital period (for a typical hot subdwarf of 0.15 $R_\odot$ and 0.5 $M_\odot$, the transit probabilities at 10 d and 50 d are about 1 and 0.35%, respectively). For each period, we explored ~30 scenarios with fine steps of 0.1 d and 0.1 $R_\oplus$, around a nominal value of the size that was previously computed with an exploration of sizes from 1 to 10 $R_\oplus$ with steps of 1 $R_\oplus$. This strategy allowed us to obtain robust estimates of the sizes with a recovery rate $\gtrsim$90% for each explored period. The total number of scenarios is considerably higher than for the full injection-and-recovery maps, as those shown in Figs. 2–4. The results from these experiments are consequently better founded than those from the full maps, which might be considered as more rough estimates of the recovery rates, but with a better and quicker general overview for small and close-in exoplanets. We do not exclude that longer-period planets might be found during our transit survey. For the tests carried out here, however, whose purpose is to quantify our potential of finding planets with a transit survey, the limit of 35 d is a good balance between the computational cost and the probability of transit. For *Kepler* data we explored one quarter, which corresponds to ~90 d of data, as well as monthly subquarters. A similar approach was adopted for K2 data, where observations usually span one campaign of ~ 80 d of data and subsamples of 30 d. Finally, for TESS data, we tested data covering one, two, three, and six sectors (27–162 d).

In all experiments, we assumed that the host star is a canonical hot subdwarf with a radius of 0.175 ± 0.025 $R_\odot$ and a mass of 0.47 ± 0.03 $M_\odot$. We considered only SC data here. We selected targets that are as unremarkable as possible, that is, nonvariable stars (i.e., no peak emerges above 4σ in a Lomb-Scargle periodogram, from pulsations, from reflection or ellipsoidal effect due to a binary nature, or from any other type of variability) with quiet (low scatter) light curves. The experiments performed here, based on the injection of synthetic transits, for computational cost reasons applied only one detrending to the resulting light curves. In all cases we used the biweight method with a nominal window-size of 2.5 h, which is large enough to cover short transits of close-in exoplanets (which have a typical duration of ~20 min) and to remove most of the stellar noise, variability, and instrumental drifts. For the actual transit search, the light curves will be detrended 12 times using either a biweight filter or a Gaussian process (Sect. 3.2), which allows us to optimize the planet search and increase the detectability of small planets. In this context, it is therefore important for our injection-and-recovery experiments here to select targets that are as quiet as possible (minimizing the need of detrending) in order to obtain results that are as representative as possible.

4.1. Results for Kepler and K2

Figure 2 (left) shows the full injection-and-recovery test for KIC 8054179 (Kp = 14.40, $G = 14.34$) from the Q6 *Kepler* data (90 days). We found that planets smaller than ~0.4 $R_\oplus$ with orbital periods longer than ~1.5 days and smaller than ~0.5 $R_\oplus$ with orbital periods longer than ~3.2 days have recovery rates below 50%, that is, we will most likely be unable to detect them (Fig. 2). For the shortest orbital periods ($\lesssim$1.5 d), objects as small as ~0.3 $R_\oplus$ are fully recovered[6]. Results from the second experiment focusing on larger planets at greater distances are presented in Table 3: the smallest planet that can be detected for 1–35 d increases from 0.3 to 1.2 $R_\oplus$ for KIC 8054179, considering 90 d of data.

We also performed similar experiments for four other representative *Kepler* targets with increasing magnitudes for one subquarter, that is, one month of data (we also provide results

[6] We explicitly checked that the detection rate of planets below ~0.3 $R_\oplus$ quickly falls below 50%.

Table 3. Minimum size of planets in units of $R_\oplus$ that can be detected in typical light curves with a $\gtrsim$90% recovery rate.

Object ID	G Mag	Data length (d)	1 d	5 d	15 d	25 d	35 d
Kepler							
8054179	14.3	90	0.3	0.5	0.8	1.0	1.2
		30	0.5	0.6	1.0	–	–
3353239	15.2	30	0.6	0.8	1.1	–	–
5938349	16.1	30	0.7	1.1	2.0	–	–
8889318	17.2	30	0.9	1.2	2.4	–	–
5342213	17.7	30	1.2	1.7	3.2	–	–
K2							
206535752	14.1	80	0.6	0.8	1.0	1.5	2.1
		30	0.6	0.9	1.6	–	–
211421561	14.9	30	0.7	1.4	1.9	–	–
228682488	16.0	30	1.0	1.4	2.5	–	–
251457058	17.1	30	1.4	2.3	3.4	–	–
248840987	18.1	30	2.1	3.3	5.4	–	–
TESS							
147283842	10.1	27	0.5	0.7	1.5	–	–
362103375	13.0	27	1.0	1.7	2.0	–	–
		162	0.7	0.8	0.9	1.0	1.3
096949372	13.0	27	1.1	1.8	2.0	–	–
441713413	13.1	27	1.3	1.7	2.0	–	–
		54	1.3	1.7	1.9	>10	>10
085400193	14.1	27	1.8	2.3	2.8	–	–
220513363	14.1	27	1.6	1.8	2.7	–	–
		81	1.3	1.6	2.5	3.0	3.0
000008842	15.0	27	2.7	3.2	4.7	–	–

Notes. All stars have $0.175 \pm 0.025\ R_\odot$ and $0.47 \pm 0.03\ M_\odot$.

for one month data for KIC 8054179, for comparison purposes). The results are presented in Table 3. For a typical *Kepler* target of 16th G magnitude (see Fig. 1), a sub-Earth-size planet of $0.7\ R_\oplus$ can still be detected at a 1 d period and a $2.0\ R_\oplus$ at 15 d period (considering one month of data).

Figure 2 (right) shows the full injection-and-recovery test for EPIC 206535752 (Kp = 13.99, $G = 14.10$), which was observed during Campaign 3 of K2 (81 days). We find that $\sim$0.6 $R_\oplus$ planets are fully recovered up to $\sim$3 d orbital periods, while the detectability of objects smaller than $0.5\ R_\oplus$ quickly drops below 50% for all orbital periods, meaning that we will likely not be able to detect them. Results from the second experiment on EPIC 206535752 focusing on larger planets at greater distances are presented in Table 3: the smallest planet that can be detected for 1 d to 35 d quickly increases from 0.6 to 2.1 $R_\oplus$, considering 80 d of data.

Similar experiments were also carried out for four other K2 targets with increasing magnitudes with a subsample of 30 d data. The results are presented in Table 3. For a typical K2 target of 15th G magnitude (see Fig. 1), a sub-Earth-size planet of $0.7\ R_\oplus$ can still be detected at a 1 d period, as can a $1.9\ R_\oplus$ at 15 d period (considering one month of data).

As a concluding remark, for a given magnitude and data duration, the *Kepler* performances are significantly superior to those of K2, although the K2 targets are generally brighter (Fig. 1 and Table 3). Almost all *Kepler* targets will allow us to detect transiting objects with a radius $\lesssim 1.0\ R_\oplus$. This is the case for about two-thirds of the K2 targets.

4.2. Results for TESS

Figure 3 presents results of injection-and-recovery tests for four stars observed in one sector by TESS. The four selected stars also are very quiet, non-variable stars. They have magnitudes of $G = 10.1$, $G = 13.0$, $G = 14.1$, and $G = 15.0$. Figure 3 shows that typically, $\sim$0.5 $R_\oplus$ ($G \sim 10.0$), $\sim$1.2 $R_\oplus$ ($G \sim 13.0$), $\sim$1.9 $R_\oplus$ ($G \sim 14.1$), and $\sim$2.7 $R_\oplus$ ($G \sim 15.0$) planets can be retrieved from TESS one-sector light curves for the shortest orbital periods with a $\gtrsim$90% recovery rate.

To appreciate the increase in detectability with multisector observations, we performed similar tests on TIC 441713413 ($G = 13.07$), which was observed in two sectors (S16 and S23), on TIC 220513363 ($G = 14.1$), which was observed in three sectors (S1, S2, and S3), and on TIC 362103375 ($G = 13.04$), which was observed in six sectors (S14, S15, S18, S22, S25, and S26). All stars were compared to results from one-sector-only tests (S16 for TIC 441713413, S1 for TIC 220513363, and S14 for TIC 362103375). Figure 4 and Table 3 present and compare the results of these experiments. The improvement in detectability from one to two sectors is barely perceptible and is noticeable only for orbital periods beyond 5 d. This is an important result because the majority of TESS targets were observed for one sector only during the primary mission (Table 1), and it will be reobserved for another one sector in the extended mission. No significant improvement in detectability obtained from the one-sector primary mission (Fig. 3) is therefore expected with one more sector data in the extended mission. The improvement from one to three sectors (TIC 220513363, see Table 3) and six sectors (TIC 362103375, see Fig. 4 and Table 3) is increasingly noticeable: We are now able to reach sub-Earth-sized objects up to 25 d with 6 sectors, for example, which was only possible for an orbital period of 1 d (and below) with one sector only.

The effect of the data length on the minimum detectable radius can be described further. In an ideal case, the longer the data set, the smaller the planet that can be detected because of the increased number of stacked transits. This improves the statistics and increases the signal-to-noise ratio (S/N). This is directly related to the working procedure of our transit-search algorithm (TLS, see Sect. 3.2). However, the real nature of the light curves, which always present a level of noise that cannot be removed, means that we do not always have a clear improvement when more transits are stacked. This is in particular the case for the short orbital periods. Adding more transits does not always yield a vast improvement, providing there is already a large number of them. This is shown in Table 3 for orbital periods of 1 d, for instance, for KIC 8054179, EPIC 206535752, and TIC 441713413. For longer orbital periods, the effect is stronger because the increase in the number of stacked transits is relatively more important. For example, for the TESS sample, the improvement in the minimum size of planets that can be detected with an orbital period of 15 d is remarkable when we expand our analysis from one sector to two (TIC 441713413), three (TIC 220513363), and six sectors (TIC 362103375).

To conclude this section, we mention that Figs. 2–4 as well as Table 3 also allow us to assess the general reliability of our results for the *Kepler*, K2, and TESS light curves. While the detectability will (unavoidably) be dependent on the target (for similar magnitude) and/or sector or quarter (for similar data length; also because of the actual radius of the host star), the general comparison of the tests carried out here shows consistent trends. For example, the results for three different stars with $G \sim 13.0$ (TIC 096949372, 362103375, and 441713413) for

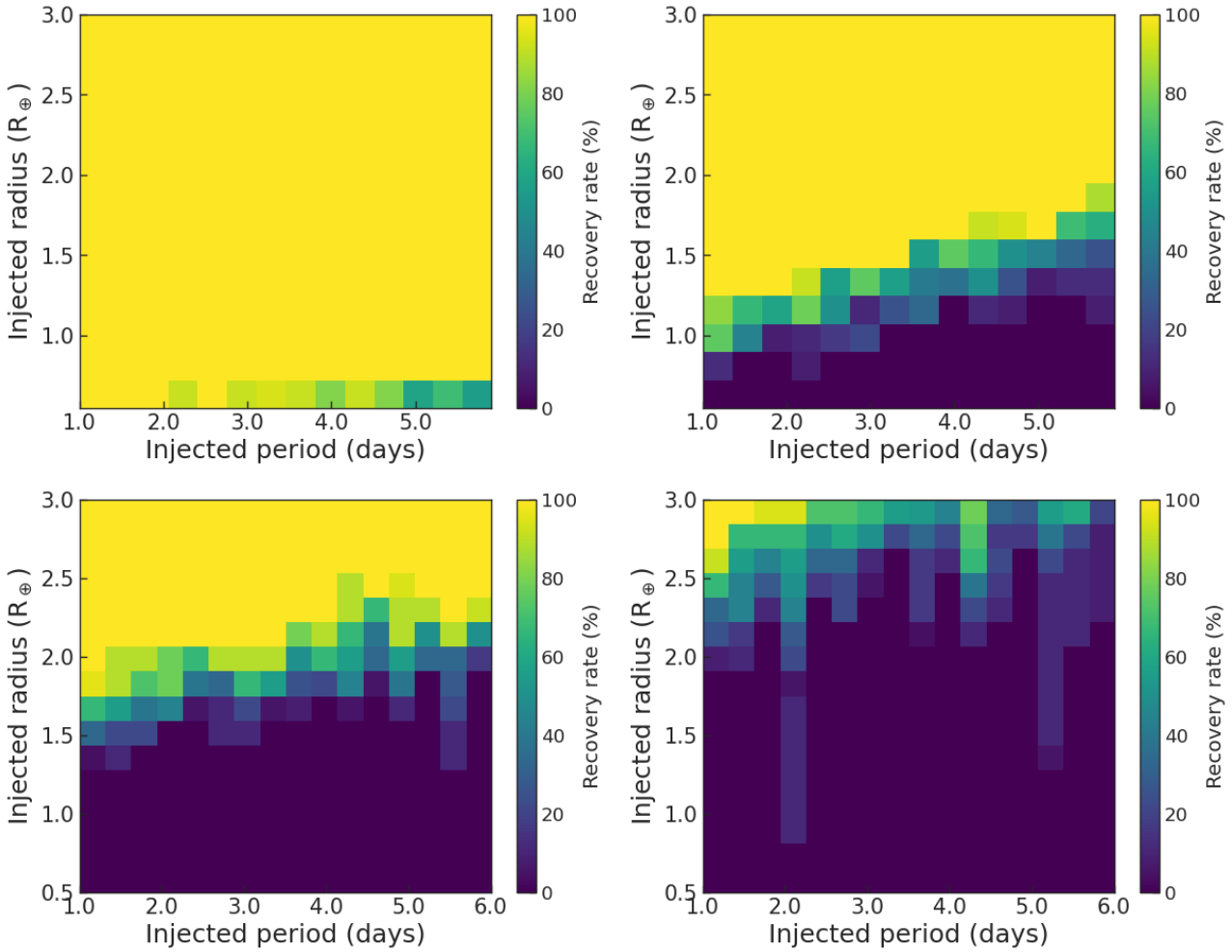

Fig. 3. Results of injection-and-recovery tests for four sdB stars observed in one sector by TESS: TIC 147283842 ($G = 10.1$, *top left panel*), TIC 96949372 ($G = 13.0$, *top right panel*), TIC 85400193 ($G = 14.1$, *bottom left panel*), and TIC 000008842 ($G = 15.0$, *bottom right panel*). 2500 injection-and-recovery tests were made for each star.

one-sector TESS data of three different sectors are globally consistent.

5. CHEOPS performances for hot subdwarfs

Figure 5 displays typical light curves obtained by CHEOPS for four representative targets: (1) HD 149382, one of the brightest known sdB stars ($G = 8.9$), which was not observed by TESS, *Kepler*, or K2; (2) CW83-1419-09 ($G = 12.0$), and (3) TYC 982-614-1 ($G = 12.2$), which represent typical CHEOPS targets in terms of magnitude; and (4) TYC 499-2297-1, a fainter target of $G = 12.6$, which exceeds the CHEOPS standard specifications. The light curves were processed using version 12 of the Data Reduction Pipeline (DRP; Hoyer et al. 2020).

These light curves were obtained with the aperture that offers the smallest root mean square of variation in count rates, which is generally the `DEFAULT` one (which has a radius of 25 arcsec). Then, we evaluated how the flux was correlated with different parameters such as the time, the CHEOPS roll angle, the x–y centroids, the background, and the contamination. This inspection was made with the `pycheops`[7] package (v0.9.6), which is developed specifically for the analysis of CHEOPS data. We thus decorrelated the light curves of any undesired trends by calculating the Bayesian information criteria (BIC) of each combination of trends under the assumption that the combination that induces the lowest BIC describes any trends best. We also removed outliers as required. After the light curves were decorrelated, we visually inspected them in the search for potential transits.

The hot subdwarf observations made by CHEOPS are fillers. This results in light curves spanning 1.5–5 h (with gaps due to Earth occultations and/or passages through the South Atlantic Anomaly, but always with an efficiency of at least 60% for an orbit, and always less than 100%) separated by several days for a given target. This makes the application of injection-and-recovery tests as conducted in Sect. 4 impractical. Our injection-and-recovery experiments were conducted with the TLS transit search tool, which is useful for long time-series observations such as those coming from *Kepler*, K2, or TESS. The power of TLS-based searching relies on the stacking of many transits, which eventually increases the S/N of a given periodic signal. However, the CHEOPS light curves are short observational data sets, in which we expect to find single transits. To characterize the CHEOPS performance for hot subdwarfs, we therefore estimated the minimum planet size based on the transit depth that could be detected with an S/N of 5 assuming a transit duration of 20 min (which is the typical duration for a ~12 h orbital period) and for various typical stellar radii from 0.15 to 0.20 $R_\odot$.

[7] https://github.com/pmaxted/pycheops

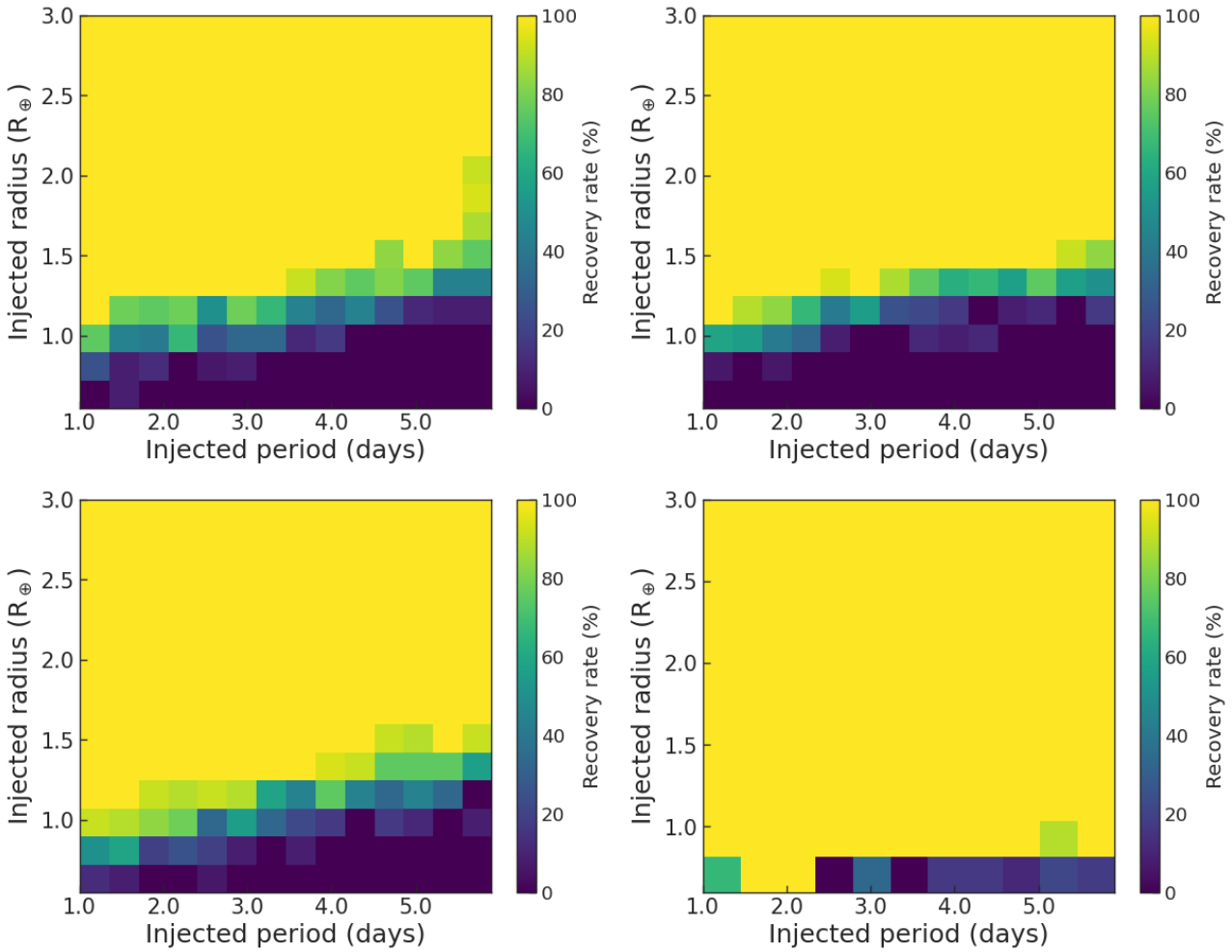

Fig. 4. Results of injection-and-recovery tests for stars observed in multiple sectors by TESS. *Top panels*: TIC 441713413 ($G = 13.07$), one-sector data (*left*) and two-sector data (*right*). *Bottom panels*: TIC 362103375 ($G = 13.04$), one-sector data (*left*) and six-sector data (*right*).

The noise of the light curve is estimated with the `pycheops` package using the scaled noise method. It assumes that the noise in the light curve is white noise with a standard error b times the error values provided by the CHEOPS DRP. We then inject transits into the light curve and find the transit depth such that the S/N of the transit depth measurement is 1. The transit model used for this noise estimate includes limb darkening, therefore we define the depth as $D = k^2$, where k is the planet-star radius ratio used to calculate the nominal model. We can use a factor s to modify the transit depth in a nominal model $\mathbf{m_0}$ calculated with approximately the correct depth to produce a new model $\mathbf{m}(s) = 1 + s \times (\mathbf{m_0} - 1)$. If the data are normalized fluxes $\mathbf{f} = f_1, \ldots, f_N$ with nominal errors $\sigma = \sigma_1, \ldots, \sigma_N$, then the log-likelihood for the model given the data is

$$\ln \mathcal{L} = -\frac{1}{2b^2}\chi^2 - \frac{1}{2}\sum_{i=1}^{N} \ln \sigma_i^2 - N \ln b - \frac{N}{2}\ln(2\pi),$$

where $\chi^2 = \sum_i^N \left(f_i - 1 - s(m_{0,i} - 1)\right)^2 / \sigma_i^2$. The maximum likelihood occurs for parameter values $\hat{s}$ and $\hat{b}$ such that $\frac{\partial \ln \mathcal{L}}{\partial s}\big|_{\hat{s},\hat{b}} = 0$ and $\frac{\partial \ln \mathcal{L}}{\partial b}\big|_{\hat{s},\hat{b}} = 0$, from which we obtain

$$\hat{s} = \sum_{i=1}^{N} \frac{(f_i - 1)(m_{0,i} - 1)}{\sigma_i^2} \left[\sum_{i=1}^{N} \frac{(m_{0,i} - 1)^2}{\sigma_i^2}\right]^{-1}$$

and

$$\hat{b} = \sqrt{\chi^2 / N}.$$

The standard errors on the eclipse depth if $s \approx 1$ are

$$\sigma_D = Db \left[\sum_{i=1}^{N} \frac{(m_i - 1)^2}{\sigma_i^2}\right]^{-1/2}.$$

Figure 6 shows the minimum planet sizes that can be detected at $S/N = 5$ for our four representative targets. For HD 149382, a ~0.4 $R_\oplus$ object (for a 0.18 $R_\odot$ host) could be detected at $S/N = 5$ if it is transiting. CW83-1419-09 and TYC 982-614-1 exhibit typical results for CHEOPS targets, reaching detections of ~0.7–0.8 $R_\oplus$ objects. Finally, the fainter TYC 499-2297-1 could allow the detection of a ~0.9 $R_\oplus$ object. The minimum planet sizes for all CHEOPS targets can be found in Table 2. They are given for a 0.18 $R_\odot$ host and for $S/N = 5$ in all cases.

Another important property to determine because of the filler nature of CHEOPS observations is which orbital periods (and for which coverage of the orbit) are reached with the existing observations. This was measured by computing the phase coverage of a hypothetical planet in a range of periods. More precisely, we computed the percentage of the phase covered for each orbital period from $P_{\rm orb} = 0.001$ d to 5 d in intervals of 0.001 d. To do

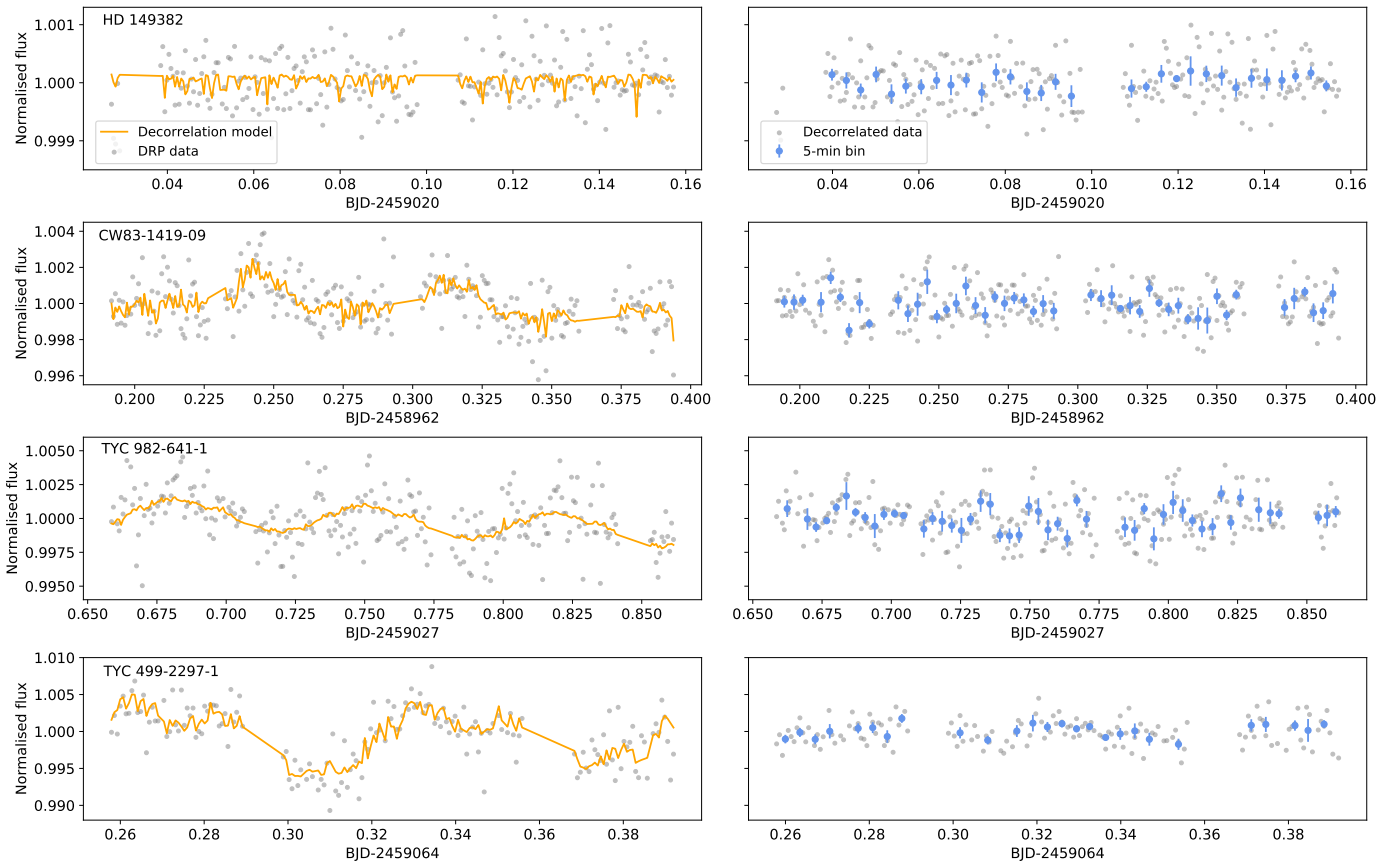

Fig. 5. Representative light curves of hot subdwarfs produced by CHEOPS. *From top to bottom*: HD 149382 ($G = 8.9$) in its fifth visit, CW83 1419-09 ($G = 12.0$) in its first visit, TYC 982-6141 ($G = 12.2$) in its fourth visit, and TYC 499-2297-1 ($G = 12.6$) in its fourth visit. In all cases, the raw light curves as processed by the DRP (gray dots) are displayed in the *left panels*, jointly with the best decorrelation model (orange line) found by means of the `pycheops` package. In the *right panels*, the decorrelated data (gray dots) with a 5-min bin (blue dots) are shown. The *y*-scale is the same for each pair of *right and left panels*.

this, we evaluated the phase coverage for a total of 5000 periods. Then, to aid interpreting the phase coverage at different periods, we binned the periods by 1.7 h. To illustrate the current status of our observational program, we estimated the period at which a phase coverage of ∼80% is reached for each target, meaning that periods equal to or shorter than this would most likely be detected if the planet exists and transits. However, even when the probabilities are low, a hypothetical planet may still reside in the unexplored phase. Results for our four representative targets are presented in Fig. 7. As of 19 December 2020, we found a phase coverage of ∼80% for orbital periods of ∼0.47 d, ∼0.39 d, ∼0.68 d, and ∼0.54 d for our four representative cases HD 149384 (7 times two orbits), CW83 1419-09 (4 times three orbits), TYC 982-614-1 (6 times three orbits), and TYC 499-2297-1 (6 times two orbits). The orbital periods reached for a phase coverage higher than 80% for the CHEOPS targets can be found in Table 2.

In light of the results of the injection-and-recovery tests in the *Kepler*, K2, and TESS light curves, all CHEOPS targets with a minimum detectable planet size greater than $\gtrsim 1.1 R_\oplus$ have been suspended (see Table 2). These targets generally have fainter magnitudes, are located in a crowded field, or have a bright close contaminating object, which explains the poorer ability of detecting planets around these objects. Another explanation is that some targets are pressure-mode (*p*-mode) sdB pulsators with a relatively high amplitude (this is the case for EC 15041-1409 and TYC 1077-218-1), which are not properly removed with our current detrending procedure (this is an improvement we aim to implement in the coming months). We instead chose to focus on the most promising targets for which planets below $\lesssim 1.1 R_\oplus$ can be detected because in these cases, CHEOPS will notably contribute to increasing the number of targets for which we could detect planetary remnants (which are likely small, possibly disintegrating objects) around post-RGB stars. From Tables 1, A.1, and B.1 and the results from Table 3, it is estimated that about 160 stars observed by *Kepler* and K2 (almost all of them for *Kepler*, and about two-thirds of them for K2) and about 50 stars from TESS (the very brightest ones, and those with $G \lesssim 13.0$ observed for at least about six sectors), will reach this minimum planet size. Statistically, only ∼40% of them are single hot subdwarfs, while in contrast, all CHEOPS targets have been chosen to be single hot subdwarfs (or, in a few cases, subdwarfs in wide binary systems) to the best of our knowledge.

The orbital periods reached by the CHEOPS filler observations will remain modest (about 1 d orbital period with a 80% phase coverage by the end of the mission for most targets). However, these results are valuable for placing constraints on the survival rates of planets that are engulfed in the envelope of their red giant host. These remnants, if present, are expected to have very short orbital periods because of the orbital decay of the orbit of the inspiraling planet inside its host star. It is noteworthy here that all of the five Earth-sized planets that are suspected around KIC 05807616 and KIC 10001893 have orbital periods of only a few hours (Charpinet et al. 2011; Silvotti et al. 2014), and

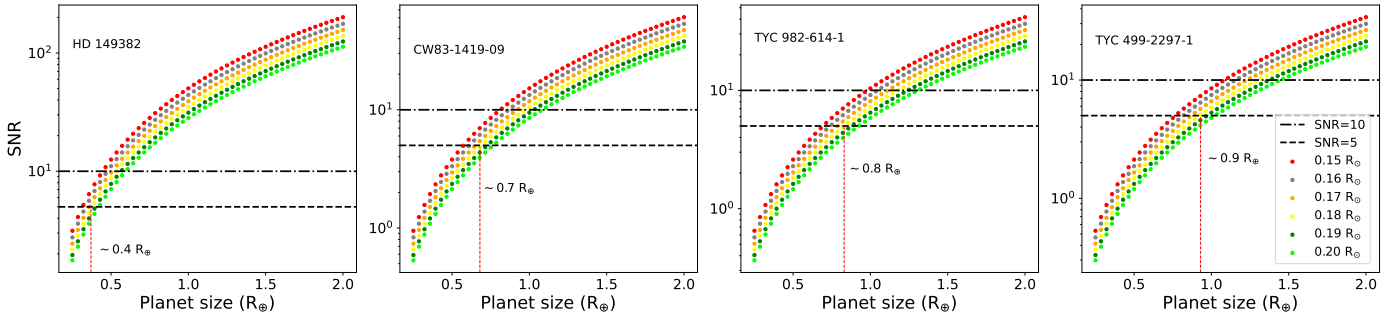

Fig. 6. Performances of CHEOPS on hot subdwarfs, assuming a single 20-min transit. *From left to right*: HD 149382 ($G = 8.9$), CW83-1419-09 ($G = 12.0$), TYC 982-614-1 ($G = 12.2$), and TYC 499-2297-1 ($G = 12.6$). The minimum planet size for an $S/N = 5$ and a 0.18 $R_\odot$ host is indicated next to the vertical red line.

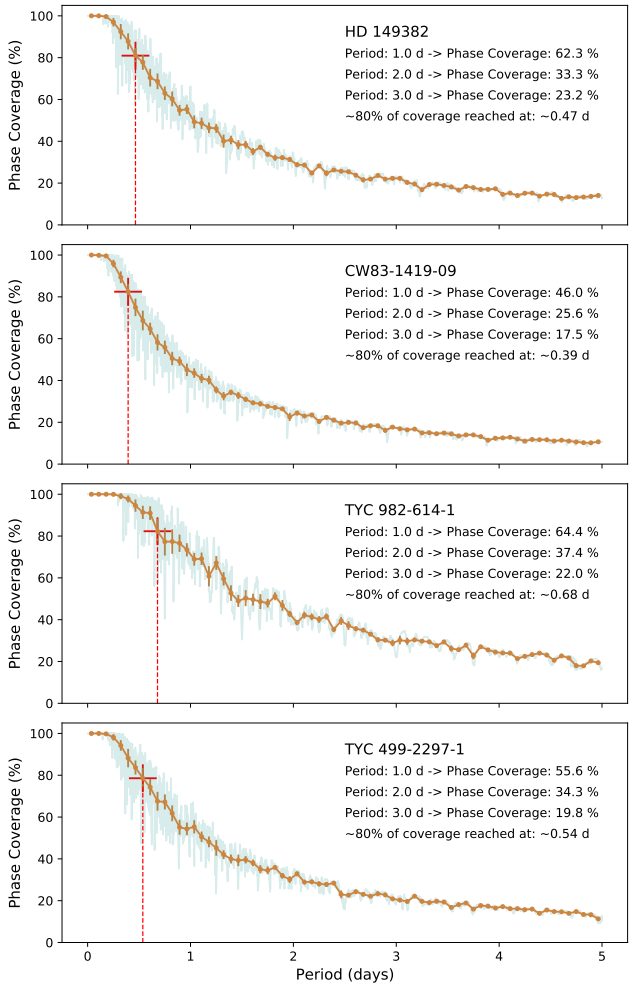

Fig. 7. Phase coverage (in percent) as a function of orbital period reached after one season of observations with CHEOPS. *From top to bottom panel*: HD 149382 (7 × 2 orbits), CW83 1419-09 (4 × 3 orbits), TYC 982-614-1 (6 × 3 orbits), and TYC 499-2297-1 (6 × 2 orbits). In all cases, the blue lines represent the full range of 5000 periods we explored, and the orange lines show the binning at each ~1.7 h. The orbital periods for which the phase coverages are ~80% are marked with dotted vertical red lines.

all known sdB+red dwarf or brown dwarf post-CE binaries have orbital periods below 1 d (Schaffenroth et al. 2018, 2019, 2021). Finally, CHEOPS provides an excellent opportunity of observing very promising targets, such as HD 149382, which have not been observed by *Kepler*, K2, or TESS.

6. Conclusions and future work

This paper presented our project that searches for transiting planets around hot subdwarfs. While no such planetary transit have been found to date, high-quality photometric light curves are now available for thousands of hot subdwarfs from the *Kepler*, K2, TESS, and CHEOPS space missions (the harvest is continuing for these last two missions). By having experienced extreme mass loss on the RGB, these small stars (0.1–0.3 $R_\odot$) constitute excellent targets based on which the question of the evolution of planetary systems directly after the first-ascent red giant branch can be addressed. Hot subdwarfs also offer the potential of observationally constraining the existence of planetary remnants, that is, planets that would have survived (even partially as a small, possibly disintegrating, very close object) being engulfed in the envelope of their red giant host star. Not only does the small star size enable the detection of small remnant objects, but the ejection of the envelope may even be the reason of the survival of such remnants by stopping the spiraling-in inside the host star. Hot subdwarfs may therefore offer the outstanding opportunity to study the interior of giant planets, whose exact structure is uncertain, even for Jupiter (Wahl et al. 2017, and refererences therein).

We first listed the hot subdwarfs observed by *Kepler*, K2, TESS, and CHEOPS. We then performed injection-and-recovery tests for a selection of representative targets from *Kepler*, K2, and TESS, with the aim to determine which transiting bodies in terms of object radius and orbital period we will be able to detect in these light curves with our tools. For CHEOPS targets, given the filler nature of the observations (they are carried out when CHEOPS has no time-constrained or higher-priority observations), we directly estimated the minimum planet size detectable from the S/N of the light curves, and then computed the orbital periods that are covered for a given phase coverage. For comparison purposes, we considered the same host star in all cases.

Objects smaller than ~1 $R_\oplus$ can be detected (if existing and transiting) for the shortest orbital periods (about 1 d and below) in most of the *Kepler*, K2, and CHEOPS targets. Values comparable to those for our Moon (~0.3 $R_\oplus$) can be achieved in the best cases. This performance of reaching sub-Earth-sized objects is obtained only for the very few brightest TESS data, as well as for stars with $G \lesssim 13$ that are observed for a significant number ($\gtrsim$6) of sectors. Altogether, we estimate that we will be able to detect planets smaller than the Earth for about 250 targets for orbital periods shorter than 1 d, if they exist. Given the relatively high probability of transits for very close objects (≈5% at 1 d orbital period), our results demonstrate that we will be able

to observationally determine whether planets are able to survive being engulfed in the envelope of their host star. Hot subdwarfs represent a short phase of stellar evolution (~150 Myr for the core-He burning, i.e., EHB, phase, and about 10% of that time for post-EHB evolution; Heber 2016), which renders the formation of second-generation planets unlikely, in particular in light of the harsh environment for planet formation around a hot subdwarf. Migration of bodies at greater distances that were not engulfed in the envelope of the red giant host would be possible for the oldest hot subdwarfs (Mustill et al. 2018), although their lifetime is likely too short for a complete circularization of the orbit. Dedicated computations will be required, as those carried out for the planets and remnants discovered around white dwarfs (Veras & Fuller 2020, and references therein).

Our tests also provided a series of representative results for the detection of larger planets at greater distances. TESS targets will provide the most important cohort for the final goal of this project, which is to provide statistically significant occurrence rates of planets as a function of object radius and orbital period around hot subdwarfs.

Our main pipeline for the search for transit events around hot subdwarfs, SHERLOCK, has already been successfully applied in a number of cases (Pozuelos et al. 2020; Demory et al. 2020). However, several implementations are being developed that are especially relevant given the nature of our targets. The first improvement involves more efficient detrending for pulsating stars (see, e.g., Sowicka et al. 2017), in particular, high-frequency p-mode hot subdwarf pulsators, which have relatively high amplitudes that can hinder the detection of shallow transits. Second, we include in SHERLOCK a model for comet-like tails of disintegrating exoplanets, which highly differ from the typical shape of transiting exoplanets (see, e.g., Brogi et al. 2012; Rappaport et al. 2012; Sanchis-Ojeda et al. 2015; Kennedy et al. 2019).

When a transit event in the light curves is identified that successfully passes all the thresholds and the vetting process, we will need to confirm the signal and associate it with a planetary nature by scheduling follow-up observations. In order to confirm transit events in light curves, we will trigger observations with our Liège TRAPPIST network (Jehin et al. 2011; Gillon et al. 2011) for the deepest signals ($\gtrsim$2500 ppm), which consists of two 0.6 m telescopes at the La Silla (Chile) and Oukaïmeden (Morocco) observatories. For shallower transits, we will directly use CHEOPS, provided the target is sufficiently well visible from the orbit of CHEOPS. When the transits are confirmed, a stellar, white dwarf, or brown dwarf origin will need to be ruled out based on RV measurements. We will first search for RV data in archives that are open to the community (such as the ESO archives) or within the hot subdwarf community. We will write proposals for appropriate spectrographs when necessary.

Finally, we will compute the occurrence rates of planets around hot subdwarfs by following a method similar to that of van Sluijs & Van Eylen (2018); Wilson et al. (2019). By comparing our results to these statistics for white dwarfs, to those for ~0.8–2.3 $M_{\odot}$ main-sequence stars that are the main progenitors of hot subdwarfs (e.g., Mayor et al. 2011; Howard et al. 2012; Fressin et al. 2013), as well as for subgiants and RGB stars (Sato et al. 2008; Döllinger et al. 2009; Jones et al. 2021), we will be able to appreciate the effect of the RGB phase alone on the evolution of exoplanetary systems.

Acknowledgements. We thank the anonymous referee for comments that improved the manuscript. The authors thank the Belgian Federal Science Policy Office (BELSPO) for the provision of financial support in the framework of the PRODEX Programme of the European Space Agency (ESA) under contract number PEA 4000131343. This work has been supported by the University of Liège through an ARC grant for Concerted Research Actions financed by the Wallonia-Brussels Federation. The authors acknowledge support from the Swiss NCCR PlanetS and the Swiss National Science Foundation. V.V.G. is a F.R.S.-FNRS Research Associate. M.G. is an F.R.S.-FNRS Senior Research Associate. St.C. acknowledges financial support from the Centre National d'Études Spatiales (CNES, France) and from the Agence Nationale de la Recherche (ANR, France) under grant ANR-17-CE31-0018. K.G.I. is the ESA CHEOPS Project Scientist and is responsible for the ESA CHEOPS Guest Observers Programme. She does not participate in, or contribute to, the definition of the Guaranteed Time Programme of the CHEOPS mission through which observations described in this paper have been taken, nor to any aspect of target selection for the programme. D.E. has received funding from the European Research Council (ERC) under the European Union's Horizon 2020 research and innovation programme (project FOUR ACES; grant agreement No 724427). This project has been carried out in the frame of the National Centre for Competence in Research PlanetS supported by the Swiss National Science Foundation (SNSF). G.B. acknowledges support from CHEOPS ASI-INAF agreement n. 2019-29-HH.0. A.J.M. acknowledges funding from the Swedish Research Council (starting grant 2017-04945) and the Swedish National Space Agency (career grant 120/19C). A.C.C. and T.G.W. acknowledge support from STFC consolidated grant number ST/M001296/1. A.B. was supported by the SNSA. M.F. gratefully acknowledge the support of the Swedish National Space Agency (DNR 65/19, 174/18). S.H. acknowledges CNES funding through the grant 837319. S.C.C.B. acknowledges support from FCT through FCT contracts nr. IF/01312/2014/CP1215/CT0004. S.G.S. acknowledge support from FCT through FCT contract nr. CEECIND/00826/2018 and POPH/FSE (EC). This work was supported by FCT - Fundação para a Ciência e a Tecnologia through national funds and by FEDER through COMPETE2020 - Programa Operacional Competitividade e Internacionalização by these grants: UID/FIS/04434/2019; UIDB/04434/2020; UIDP/04434/2020; PTDC/FIS-AST/32113/2017 & POCI-01-0145-FEDER-032113; PTDC/FIS-AST/28953/2017 & POCI-01-0145-FEDER-028953; PTDC/FIS-AST/28987/2017 & POCI-01-0145-FEDER-028987. O.D.S.D. is supported in the form of work contract (DL 57/2016/CP1364/CT0004) funded by national funds through FCT. B.-O.D. acknowledges support from the Swiss National Science Foundation (PP00P2-190080). B.N.B. acknowledges funding through the TESS Guest Investigator Program Grant 80NSSC21K0364. We acknowledge support from the Spanish Ministry of Science and Innovation and the European Regional Development Fund through grants ESP2016-80435-C2-1-R, ESP2016-80435-C2-2-R, PGC2018-098153-B-C33, PGC2018-098153-B-C31, ESP2017-87676-C5-1-R, MDM-2017-0737 Unidad de Excelencia "María de Maeztu"- Centro de Astrobiología (INTA-CSIC), as well as the support of the Generalitat de Catalunya/CERCA programme. The MOC activities have been supported by the ESA contract No. 4000124370. I.R. acknowledges support from the Spanish Ministry of Science and Innovation and the European Regional Development Fund through grant PGC2018-098153-B-C33, as well as the support of the Generalitat de Catalunya/CERCA programme. X.B., Se.C., D.G., M.F. and J.L. acknowledge their role as ESA-appointed CHEOPS science team members. D.G. gratefully acknowledges financial support from the CRT foundation under Grant No. 2018.2323 "Gaseous or rocky? Unveiling the nature of small worlds". P.F.L.M. acknowledges support from STFC research grant number ST/M001040/1. This project has been supported by the Hungarian National Research, Development and Innovation Office (NKFIH) grants GINOP-2.3.2-15-2016-00003, K-119517, K-125015, and the City of Szombathely under Agreement No. 67.177-21/2016. This paper includes data collected by the TESS mission. Funding for the TESS mission is provided by the NASA Explorer Program. Funding for the TESS Asteroseismic Science Operations Centre is provided by the Danish National Research Foundation (Grant agreement no.: DNRF106), ESA PRODEX (PEA 4000119301) and Stellar Astrophysics Centre (SAC) at Aarhus University. We thank the TESS team and staff and TASC/TASOC for their support of the present work. This work has made use of data from the ESA mission *Gaia* (https://www.cosmos.esa.int/gaia), processed by the *Gaia* Data Processing and Analysis Consortium (DPAC, https://www.cosmos.esa.int/web/gaia/dpac/consortium). Funding for the DPAC has been provided by national institutions, in particular the institutions participating in the *Gaia* Multilateral Agreement.

References

Allard, F., Wesemael, F., Fontaine, G., Bergeron, P., & Lamontagne, R. 1994, AJ, 107, 1565

Aller, A., Lillo-Box, J., Jones, D., Miranda, L. F., & Barceló Forteza, S. 2020, A&A, 635, A128

Baglin, A., Auvergne, M., Boisnard, L., et al. 2006, in 36th COSPAR Scientific Assembly, 36, 3749

Baran, A. S., Zola, S., Blokesz, A., Østensen, R. H., & Silvotti, R. 2015, A&A, 577, A146
Benz, W., Broeg, C., Fortier, A., et al. 2021, Exp. Astron., 51, 109
Beuermann, K., Dreizler, S., Hessman, F. V., & Deller, J. 2012, A&A, 543, A138
Blokesz, A., Krzesinski, J., & Kedziora-Chudczer, L. 2019, A&A, 627, A86
Borucki, W. J., Koch, D., Basri, G., et al. 2010, Science, 327, 977
Bours, M. C. P., Marsh, T. R., Parsons, S. G., et al. 2016, MNRAS, 460, 3873
Brogi, M., Keller, C. U., de Juan Ovelar, M., et al. 2012, A&A, 545, L5
Campante, T. L., Corsaro, E., Lund, M. N., et al. 2019, ApJ, 885, 31
Charpinet, S., Green, E. M., Baglin, A., et al. 2010, A&A, 516, L6
Charpinet, S., Fontaine, G., Brassard, P., et al. 2011, Nature, 480, 496
Charpinet, S., Giammichele, N., Zong, W., et al. 2018, Open Astron., 27, 112
Debes, J. H., & Sigurdsson, S. 2002, ApJ, 572, 556
Demory, B. O., Pozuelos, F. J., Gómez Maqueo Chew, Y., et al. 2020, A&A, 642, A49
Döllinger, M. P., Hatzes, A. P., Pasquini, L., Guenther, E. W., & Hartmann, M. 2009, A&A, 505, 1311
Dorman, B., Rood, R. T., & O'Connell, R. W. 1993, ApJ, 419, 596
Eisner, N., Lintott, C., & Aigrain, S. 2020, J. Open Source Softw., 5, 2101
Fontaine, G., Brassard, P., Charpinet, S., et al. 2012, A&A, 539, A12
Fressin, F., Torres, G., Charbonneau, D., et al. 2013, ApJ, 766, 81
Fulton, B. J., Tonry, J. L., Flewelling, H., et al. 2014, ApJ, 796, 114
Gaia Collaboration (Brown, A. G. A., et al.) 2018, A&A, 616, A1
Gänsicke, B. T., Schreiber, M. R., Toloza, O., et al. 2019, Nature, 576, 61
Geier, S. 2020, A&A, 635, A193
Geier, S., Edelmann, H., Heber, U., & Morales-Rueda, L. 2009, ApJ, 702, L96
Geier, S., & Heber, U. 2012, A&A, 543, A149
Giacalone, S., Dressing, C. D., Jensen, E. L. N., et al. 2021, AJ, 161, 24
Gillon, M., Jehin, E., Magain, P., et al. 2011, EPJ Web Conf., 11, 06002
Günther, M. N., & Daylan, T. 2019, Astrophysics Source Code Library [record ascl:1903.003]
Günther, M. N., & Daylan, T. 2021, ApJS, 254, 13
Günther, M. N., Pozuelos, F. J., Dittmann, J. A., et al. 2019, Nat. Astron., 3, 1099
Han, Z., Podsiadlowski, P., Maxted, P. F. L., Marsh, T. R., & Ivanova, N. 2002, MNRAS, 336, 449
Han, Z., Podsiadlowski, P., Maxted, P. F. L., & Marsh, T. R. 2003, MNRAS, 341, 669
Heber, U. 1986, A&A, 155, 33
Heber, U. 2016, PASP, 128, 082001
Hippke, M., & Heller, R. 2019, A&A, 623, A39
Hippke, M., David, T. J., Mulders, G. D., & Heller, R. 2019, AJ, 158, 143
Hollands, M. A., Gänsicke, B. T., & Koester, D. 2018, MNRAS, 477, 93
Howard, A. W., Marcy, G. W., Bryson, S. T., et al. 2012, ApJS, 201, 15
Howell, S. B., Sobeck, C., Haas, M., et al. 2014, PASP, 126, 398
Hoyer, S., Guterman, P., Demangeon, O., et al. 2020, A&A, 635, A24
Iben, I. J. 1990, ApJ, 353, 215
Jehin, E., Gillon, M., Queloz, D., et al. 2011, The Messenger, 145, 2
Jones, M. I., Wittenmyer, R., Aguilera-Gómez, C., et al. 2021, A&A, 646, A131
Kennedy, G. M., Hope, G., Hodgkin, S. T., & Wyatt, M. C. 2019, MNRAS, 482, 5587
Kostov, V. B., Schlieder, J. E., Barclay, T., et al. 2019, AJ, 158, 32
Kovács, G., Zucker, S., & Mazeh, T. 2002, A&A, 391, 369
Krzesinski, J. 2015, A&A, 581, A7
Lee, J. W., Kim, S.-L., Kim, C.-H., et al. 2009, AJ, 137, 3181
Lutz, R., Schuh, S., & Silvotti, R. 2012, Astron. Nachr., 333, 1099
Mackebrandt, F., Schuh, S., Silvotti, R., et al. 2020, A&A, 638, A108
Maldonado, R. F., Villaver, E., Mustill, A. J., Chávez, M., & Bertone, E. 2021, MNRAS, 501, L43
Marsh, T. R. 2018, Circumbinary Planets Around Evolved Stars, eds. H. J. Deeg, & J. A. Belmonte (Berlin: Springer), 96
Maxted, P. f. L., Heber, U., Marsh, T. R., & North, R. C. 2001, MNRAS, 326, 1391
Mayor, M., Marmier, M., Lovis, C., et al. 2011, ArXiv e-prints [arXiv:1109.2497]
Miglio, A., Brogaard, K., Stello, D., et al. 2012, MNRAS, 419, 2077
Miller Bertolami, M. M., Althaus, L. G., Unglaub, K., & Weiss, A. 2008, A&A, 491, 253
Mosser, B., Goupil, M. J., Belkacem, K., et al. 2012, A&A, 548, A10
Mustill, A. J., Veras, D., & Villaver, E. 2014, MNRAS, 437, 1404
Mustill, A. J., Villaver, E., Veras, D., Gänsicke, B. T., & Bonsor, A. 2018, MNRAS, 476, 3939
Norris, J. M., Wright, J. T., Wade, R. A., Mahadevan, S., & Gettel, S. 2011, ApJ, 743, 88
Nowak, G., Luque, R., Parviainen, H., et al. 2020, A&A, 642, A173
Østensen, R. H., Silvotti, R., Charpinet, S., et al. 2010, MNRAS, 409, 1470
Østensen, R. H., Silvotti, R., Charpinet, S., et al. 2011, MNRAS, 414, 2860
Pablo, H., Kawaler, S. D., & Green, E. M. 2011, ApJ, 740, L47
Pelisoli, I., Vos, J., Geier, S., Schaffenroth, V., & Baran, A. S. 2020, A&A, 642, A180
Pozuelos, F. J., Suárez, J. C., de Elía, G. C., et al. 2020, A&A, 641, A23
Pulley, D., Faillace, G., Smith, D., Watkins, A., & Owen, C. 2015, J. British Astrono. Assoc., 125, 284
Qian, S. B., Zhu, L. Y., Dai, Z. B., et al. 2012, ApJ, 745, L23
Quinn, S. N., Becker, J. C., Rodriguez, J. E., et al. 2019, AJ, 158, 177
Rappaport, S., Levine, A., Chiang, E., et al. 2012, ApJ, 752, 1
Ratzloff, J. K., Barlow, B. N., Kupfer, T., et al. 2019, ApJ, 883, 51
Reindl, N., Geier, S., Kupfer, T., et al. 2016, A&A, 587, A101
Ricker, G. R., Winn, J. N., Vanderspek, R., et al. 2014, SPIE Conf. Ser., 9143, 914320
Saffer, R. A., Bergeron, P., Koester, D., & Liebert, J. 1994, ApJ, 432, 351
Saio, H., & Jeffery, C. S. 2000, MNRAS, 313, 671
Saio, H., & Jeffery, C. S. 2002, MNRAS, 333, 121
Sanchis-Ojeda, R., Rappaport, S., Pallè, E., et al. 2015, ApJ, 812, 112
Sato, B., Toyota, E., Omiya, M., et al. 2008, PASJ, 60, 1317
Schaffenroth, V., Geier, S., Heber, U., et al. 2018, A&A, 614, A77
Schaffenroth, V., Barlow, B. N., Geier, S., et al. 2019, A&A, 630, A80
Schaffenroth, V., Casewell, S. L., Schneider, D., et al. 2021, MNRAS, 501, 3847
Schleicher, D. R. G., & Dreizler, S. 2014, A&A, 563, A61
Schneider, D., Heber, U., Geier, S., Latour, M., & Irrgang, A. 2019, https://doi.org/10.5281/zenodo.3428841
Silvotti, R., Schuh, S., Janulis, R., et al. 2007, Nature, 449, 189
Silvotti, R., Charpinet, S., Green, E., et al. 2014, A&A, 570, A130
Silvotti, R., Schuh, S., Kim, S. L., et al. 2018, A&A, 611, A85
Silvotti, R., Ostensen, R. H., & Telting, J. H. 2020, ArXiv e-prints [arXiv:2002.04545]
Sowicka, P., Handler, G., Dębski, B., et al. 2017, MNRAS, 467, 4663
Stark, M. A., & Wade, R. A. 2003, AJ, 126, 1455
Stassun, K. G., Oelkers, R. J., Paegert, M., et al. 2019, AJ, 158, 138
van Sluijs, L., & Van Eylen, V. 2018, MNRAS, 474, 4603
Van Grootel, V., Charpinet, S., Brassard, P., Fontaine, G., & Green, E. M. 2013, A&A, 553, A97
Van Eylen, V., Albrecht, S., Gandolfi, D., et al. 2016, AJ, 152, 143
Vanderburg, A., Johnson, J. A., Rappaport, S., et al. 2015, Nature, 526, 546
Vanderburg, A., Rappaport, S. A., Xu, S., et al. 2020, Nature, 585, 363
Veras, D., & Fuller, J. 2020, MNRAS, 492, 6059
Völschow, M., Banerjee, R., & Hessman, F. V. 2014, A&A, 562, A19
Vos, J., Németh, P., Vučković, M., Østensen, R., & Parsons, S. 2018, MNRAS, 473, 693
Wahl, S. M., Hubbard, W. B., Militzer, B., et al. 2017, Geophys. Res. Lett., 44, 4649
Webbink, R. F. 1984, ApJ, 277, 355
Welsh, W. F., Orosz, J. A., Carter, J. A., et al. 2012, Nature, 481, 475
Wilson, T. G., Farihi, J., Gänsicke, B. T., & Swan, A. 2019, MNRAS, 487, 133
Wittenmyer, R. A., Horner, J., & Marshall, J. P. 2013, MNRAS, 431, 2150
Zhang, X., & Jeffery, C. S. 2012, MNRAS, 419, 452
Zhu, L.-Y., Qian, S.-B., Fernández Lajús, E., Wang, Z.-H., & Li, L.-J. 2019, Res. Astron. Astrophys., 19, 134
Zorotovic, M., & Schreiber, M. R. 2013, A&A, 549, A95

[1] Space sciences, Technologies and Astrophysics Research (STAR) Institute, Université de Liège, 19C Allée du 6 Août, 4000 Liège, Belgium
e-mail: valerie.vangrootel@uliege.be
[2] Astrobiology Research Unit, Université de Liège, Allée du 6 Août 19C, 4000 Liège, Belgium
[3] Institut de Recherche en Astrophysique et Planétologie, CNRS, Université de Toulouse, CNES, 14 avenue Edouard Belin, 31400 Toulouse, France
[4] Observatoire Astronomique de l'Université de Genève, Chemin Pegasi 51, Versoix, Switzerland
[5] Physikalisches Institut, University of Bern, Gesellsschaftstrasse 6, 3012 Bern, Switzerland
[6] Center for Space and Habitability, Gesellsschaftstrasse 6, 3012 Bern, Switzerland
[7] Aix Marseille Univ, CNRS, CNES, LAM, Marseille, France
[8] Instituto de Astrofísica e Ciências do Espaço, Universidade do Porto, CAUP, Rua das Estrelas, 4150-762 Porto, Portugal
[9] Department of Physics, High Point University, One University Parkway, High Point, NC 27268, USA
[10] Universidad Internacional de Valencia (VIU), Carrer del Pintor Sorolla 21, 46002 Valencia, Spain

[11] Dpto. Física Teórica y del Cosmos, Universidad de Granada, 18071 Granada, Spain
[12] Department of Physics, Astronomy and Materials Science, Missouri State University, 901 S. National, Springfield, MO 65897, USA
[13] Instituto de Astrofísica de Canarias, 38200 La Laguna, Tenerife, Spain
[14] Departamento de Astrofísica, Universidad de La Laguna, 38206 La Laguna, Tenerife, Spain
[15] Institut de Ciències de l'Espai (ICE, CSIC), Campus UAB, Can Magrans s/n, 08193 Bellaterra, Spain
[16] Institut d'Estudis Espacials de Catalunya (IEEC), 08034 Barcelona, Spain
[17] ESTEC, European Space Agency, 2201AZ, Noordwijk, NL, The Netherlands
[18] Depto. de Astrofísica, Centro de Astrobiologia (CSIC-INTA), ESAC campus, 28692 Villanueva de la Cãda (Madrid), Spain
[19] Departamento de Física e Astronomia, Faculdade de Ciências, Universidade do Porto, Rua do Campo Alegre, 4169-007 Porto, Portugal
[20] Space Research Institute, Austrian Academy of Sciences, Schmiedlstrasse 6, 8042 Graz, Austria
[21] Université Grenoble Alpes, CNRS, IPAG, 38000 Grenoble, France
[22] Department of Astronomy, Stockholm University, AlbaNova University Center, 10691 Stockholm, Sweden
[23] INAF, Osservatorio Astrofisico di Catania, Via S. Sofia 78, 95123 Catania, Italy
[24] ADMATIS, 3534 Miskolc, Kandó Kálmán u. 5., Hungary
[25] Institute of Planetary Research, German Aerospace Center (DLR), Rutherfordstrasse 2, 12489 Berlin, Germany
[26] Centre for Exoplanet Science, SUPA School of Physics and Astronomy, University of St Andrews, North Haugh, St Andrews KY16 9SS, UK
[27] Université de Paris, Institut de physique du globe de Paris, CNRS, 75005 Paris, France
[28] Lund Observatory, Dept. of Astronomy and Theoretical Physics, Lund University, Box 43, 22100 Lund, Sweden
[29] Leiden Observatory, University of Leiden, PO Box 9513, 2300 RA Leiden, The Netherlands
[30] Department of Space, Earth and Environment, Chalmers University of Technology, Onsala Space Observatory, 43992 Onsala, Sweden
[31] Dipartimento di Fisica, Università degli Studi di Torino, via Pietro Giuria 1, 10125 Torino, Italy
[32] University of Vienna, Department of Astrophysics, Türkenschanzstrasse 17, 1180 Vienna, Austria
[33] Department of Physics, University of Warwick, Gibbet Hill Road, Coventry CV4 7AL, UK
[34] Konkoly Observatory, Research Centre for Astronomy and Earth Sciences, 1121 Budapest, Konkoly Thege Miklós út 15-17, Hungary
[35] ELTE Eötvös Loránd University, Institute of Physics, Pázmány Péter sétány 1/A, 1117 Budapest, Hungary
[36] Sydney Institute for Astronomy, School of Physics A29, University of Sydney, NSW 2006, Australia
[37] IMCCE, UMR8028 CNRS, Observatoire de Paris, PSL Univ., Sorbonne Univ., 77 av. Denfert-Rochereau, 75014 Paris, France
[38] Institut d'astrophysique de Paris, UMR7095 CNRS, Université Pierre & Marie Curie, 98bis blvd. Arago, 75014 Paris, France
[39] INAF, Osservatorio Astronomico di Padova, Vicolo dell'Osservatorio 5, 35122 Padova, Italy
[40] Astrophysics Group, Keele University, Staffordshire, ST5 5BG, UK
[41] Institute of Optical Sensor Systems, German Aerospace Center (DLR), Rutherfordstrasse 2, 12489 Berlin, Germany
[42] Dipartimento di Fisica e Astronomia, Università degli Studi di Padova, Vicolo dell'Osservatorio 3, 35122 Padova, Italy
[43] Centre Spatial de Liège, STAR institute, Université de Liège, avenue du Pré Aily, 4031 Angleur (Liège), Belgium
[44] Cavendish Laboratory, JJ Thomson Avenue, Cambridge CB3 0HE, UK
[45] Center for Astronomy and Astrophysics, Technical University Berlin, Hardenberstrasse 36, 10623 Berlin, Germany
[46] Institut für Geologische Wissenschaften, Freie Universität Berlin, 12249 Berlin, Germany
[47] INAF – Osservatorio Astrofisico di Torino, Strada dell'Osservatorio 20, 10025 Pino Torinese, Italy
[48] ELTE Eötvös Loránd University, Gothard Astrophysical Observatory, 9700 Szombathely, Szent Imre h. u. 112, Hungary
[49] MTA-ELTE Exoplanet Research Group, 9700 Szombathely, Szent Imre h. u. 112, Hungary
[50] Institute of Astronomy, University of Cambridge, Madingley Road, Cambridge, CB3 0HA, UK

Appendix A: Hot subdwarfs observed in the original *Kepler* field

Table A.1. Hot subdwarfs observed in the original *Kepler* field.

KIC	Class	Other name	Kp	Quarters (SC)	Quarters (LC)
sdB pulsators					
9 472 174	sdB+dM	2M1938+4603	12.3	Q0, Q5-Q17.2	All: Q0-Q17.2
2 437 937	sdB	B5 (NGC6791)	13.9	Q11.X	Q11
3 527 751	sdB	J19036+3836	14.8	Q2, Q5-Q17.2	Idem SC
11 558 725	sdB+WD	J19265+4930	14.9	Q3.3, Q6-Q17.2	Q3, Q5-Q17.2
5 807 616	sdB	KPD 1943+4058	15.0	Q2.3, Q5-Q17.2	Idem SC
10 553 698	sdB	J19531+4743	15.1	Q4.1, Q8-Q10, Q12-Q14, Q16-Q17.2	Q4-Q6, Q8-Q10, Q12-Q17.2
2 697 388	sdB	J19091+3756	15.4	Q2.3, Q5-Q17.2	Idem SC
7 668 647	sdB+WD	FBS1903+432	15.4	Q3.1, Q6-Q17.2	Q3.1, Q5-Q17.2
10 001 893	sdB	J19095+4659	15.8	Q3.2, Q6-Q17.2	Q3.2, Q5-Q17.2
10 139 564	sdB	J19249+4707	16.1	Q2.1, Q5-Q17.2	Idem SC
8 302 197	sdB	J19310+4413	16.4	Q3.1, Q5-Q17.2 except Q12	idem SC
7 664 467	sdB	J18561+4319	16.4	Q2.3, Q5-Q17.2 except Q12	idem SC
10 670 103	sdB	J19346+4758	16.5	Q2.3, Q5-Q17.2	Idem SC
11 179 657	sdB+dM	J19023+4850	17.1	Q2.3, Q5-Q17.2 except Q8 and Q12	idem SC
2 991 403	sdB+dM	J19272+3808	17.1	Q1, Q5-Q17.2	Idem SC
2 991 276	sdB	J19271+3810	17.4	Q2.1, Q6-Q17.2 except Q12	Idem SC
2 569 576	sdB	B3 (NGC6791)	18.1	Q11.3, Q14-Q17.2	Q11, Q14-Q17.2
2 438 324	sdB+dM	B4 (NGC6791)	18.3	Q6-Q17.2	Idem SC
sdB/sdOB non pulsators					
6 848 529	sdB+?	BD +42 3250	10.7	Q0	All: Q0-Q17.2
1 868 650	sdB+dM	KBS 13	13.4	Q1	All: Q0-Q17.2
9 543 660	sdOB		13.8	Q1	Q1-Q17, except Q7 and Q11
10 982 905	sdB+F/G	J19405+4827	14.1	Q2.1	Q2-Q10
6 188 286	sdOB		14.2	Q2.3	Q2, Q6-Q8, Q14-Q16
8 054 179	He-sdOB		14.4	Q3.1, Q6	Q3.1, Q4-Q17.2 except Q11 and Q12
7 975 824	sdOB+WD	KPD 1946+4340	14.6	Q1, Q5-Q12	Q1, Q5-Q17.2
10 449 976	He-sdOB		14.9	Q3.2	Q3, Q5-Q9
3 353 239	sdB		15.2	Q4.1	Q4-Q5, Q7-Q9, Q13-Q17
10 593 239	sdB+F/G	J19162+4749	15.3	Q2.3	Q2, Q5-Q17.2
2 569 583	sdB	B6 (NGC6791)	15.4	Q11.2	Q11
7 104 168	sdB		15.5	Q3.1	Q3, Q5-Q9
10 149 211	sdB+?		15.5	Q4.2	Q4-Q17.2
10 789 011	sdOB		15.5	Q3.2	Q3, Q5-Q10
11 350 152	sdB+F/G		15.5	Q3.1	Q3, Q5-Q10
7 434 250	sdB+?	J19135+4302	15.5	Q2.3	Q2, Q5-Q17.2
2 020 175	sdB		15.5	Q3.1	Q3, Q5-Q10, Q13-Q17.2
12 021 724	sdB+WD?		15.6	Q4.2	Q4-Q10
3 343 613	He-sdOB		15.7	Q3.2	Q3, Q5-Q10
5 938 349	sdB		16.1	Q3.2	Q3, Q10
6 614 501	sdB+WD?		16.1	Q3.3, Q5, Q6, Q8-Q10	Q3.3, Q5-Q17.2
9 211 123	sdB		16.1	Q3.3	Q3, Q5-Q10, Q13-Q17.2
9 957 741	He-sdOB		16.1	Q2.1	Q2, Q6-Q9
2 304 943	sdB		16.2	Q3.3	Q3, Q10
8 496 196	sdOB		16.4	Q2.3	Q2, Q6-Q10
8 874 184	sdB+?		16.5	Q4.1	Q4-Q10, Q13-Q17.2
8 022 110	sdB		16.5	Q2.3	Q2, Q6-Q10, Q13-Q17.2
6 878 288	He-sdOB+?		16.7	Q3.1	Q3, Q5-Q10
6 522 967	sdB		16.9	Q3.2	Q3, Q10
7 799 884	sdB		16.9	Q4.1	Q4.1
10 462 707	sdB+WD?		16.9	Q4.1	Q4.1, Q10
11 400 959	sdB		16.9	Q4.1	Q4.1
10 784 623	sdB		17.0	Q10	Q4-Q10 except Q8
10 961 070	sdOB		17.0	Q4.2	Q4.2
3 527 028	sdB+?		17.1	Q4.2	Q4-Q10
5 340 370	sdB+?		17.1	Q4.2	Q4, Q10
9 569 458	sdB		17.2	Q1	Q1
8 889 318	sdB		17.2	Q2.3	Q2.3, Q13-Q17.2
9 408 967	He-sdOB		17.2	Q2.3	Q2.3, Q10
4 244 427	sdB		17.3	Q2.1, Q6-Q10	Q2.1, Q6-Q17.2 except Q12
8 142 623	sdB+?	J18427+4404	17.3	Q1	Q1, Q5-Q17.2
11 357 853	sdOB		17.4	Q2.1	Q2.1
3 527 617	He-sdOB		17.5	Q2.2	Q2.2
3 729 024	sdB		17.6	Q2.2	Q2.2
9 095 594	sdB		17.7	Q3.2	Q3.2
5 342 213	sdOB		17.7	Q2.2	Q2.2, Q14-Q16
10 661 778	sdB		17.7	Q2.3, Q6-Q10	Q2.3, Q6-Q17.2 except Q11 and Q12
sdO non pulsators					
7 755 741	sdO		13.7	Q1	Q1-Q17
9 822 180	sdO+F/G		14.6	Q2.1, Q6	Q2.1, Q6-Q10
7 353 409	sdO		14.7	Q2.2, Q5	Q2.2, Q5-Q9
10 207 025	He-sdO		15.0	Q3.3	Q3.3, Q5-Q9
7 335 517	sdO+dM		15.7	Q3.2, Q6	Q3.2, Q5-Q17.2
2 297 488	sdO+F/G		17.2	Q1	Q1
2 303 576	He-sdO+?		17.4	Q3.3, Q6	Q3.3, Q6-Q17.2

Notes. Commissioning (9.7 days starting 2 May 2009): Q0; survey phase: Q1: 33.5 d (12 May–14 June 2009), Q2, Q3, and Q4: about 90 days each, divided in 3, i.e., monthly surveys; rest of the mission: Q5–Q16: about 90 days each; mission stopped at Q17.2 (11 May 2013).

Appendix B: List of hot subdwarfs observed in the K2 fields

Table B.1. Hot subdwarfs observed in the K2 fields.

KIC	Class	Other name	Kp	Campaign (SC)	Campaign (LC)
sdB pulsators					
220 641 886	sdB	HD 4539	10.40	8	8
228 755 638	sdB+dM	HW Vir	10.76	10 (101-102)	10 (101-102)
211 623 711	He-sdB	UVO 0825+15	11.89	5;18	5;18
220 376 019	sdB+WD	PG 0101+039	12.11	8	8
220 422 705	sdB+G	PG 0039+049	12.87	8	8
249 942 493	sdB	EC 15 103-1557	12.89	15	15
211 779 126	sdB	2M0856+1701	12.92	5;18	5;18
246 387 816	sdB+dM	EQ Psc	12.92	12	12
246 023 959	sdB+dM	PHL 457	13.04	12	12
211 881 419	iHe-sdB	PG 0848+186	13.30	16;18	5;16;18
201 203 416	sdB	PG 1156-037	13.46	10 (101-102)	10 (101-102)
248 411 044	sdB	UY Sex	13.56	14	14
246 141 920	sdB	PHL 531	13.99	12	12
211 433 013	sdB+WD	LT Cnc	14.02	16	16
211 765 471	sdB+WD	HZ Cnc	14.04	5;16;18	5;16;18
220 614 972	sdB+F	PG 0048+091	14.29	8	8
211 392 098	sdB+MS	SDSS J082517.99+113106.3	14.34	18	5;18
211 437 457	sdB	PG 0902+124	14.73	16	16
246 683 636	sdB+dM	V1405 Ori	15.07	13	13
248 368 659	sdB+WD	VPHAS J181343.0-213 843.9	15.10	9 (91-92)	9 (91-92)
212 508 753	sdB+F7	PG 1315-123	15.13	6;17	6;17
211 823 779	sdB+F1	SDSS J082003.35+173914.2	15.22	5;18	5;18
212 475 716	sdB+MS	EC 13 356-1300	15.24	17	17
211 696 659	sdB+WD	SDSS J083603.98+155216.4	15.50	5;18	5;18
212 707 862	sdB	SDSS J135544.71-080354.3	15.55	6;17	6;17
212 204 284	sdB	PG 0843+246	15.64	16	16
246 283 223	sdB	HE 2307-0340	15.66	12	12
248 368 658	sdB		15.70	9 (91-92)	9 (91-92)
218 717 602	sdB		15.76	7	7
211 938 328	sdB+F6	LB 378	15.78	5;18	5;18
218 366 972	sdB+WD		15.94	7	7
201 206 621	sdB+WD	PG 1142-037	15.99	1	1
212 487 276	sdB	EC 13 359-1245	16.23	17	17
217 280 630	sdB		16.33	7	7
215 776 487	sdB		16.35	7	7
203 948 264	sdB		16.70	2	2
246 373 305	iHe-sdB	PHL 417	16.88	12	12
251 668 197	sdB	EC 15 094-1725	17.00	15	15
229 002 689	sdB	SDSS J122057.48-012642.3	18.65	10 (101-102)	10 (101-102)
220 188 903	sdB+WD	PB 6373	14.91	no data	8
230 195 595	sdB		15.59	no data	11
sdB/sdOB non pulsators, single					
234 319 842	sdB		12.97	11 (111-112)	11 (111-112)
60 017 832	sdB	PG 2349+002	13.27	T	
211 708 181	sdB	GALEX J081233.6+160121	13.77	5	5
227 389 858	sdB		13.79	11 (111-112)	11 (111-112)
246 230 928	sdB	PHL 529	13.93	12	12
206 535 752	sdB	PHL 358	13.99	3	3
201 648 341	sdB	PG 1214+031	14.04	10 (101-102)	10 (101-102)
217 204 898	sdB		14.26	7	7
246 643 895	sdB	HS 0446+1344	14.50	13	13
212 722 777	sdB	PG 1330-074	14.93	17	17
211 727 748	sdB	PG 0838+165	14.99	5;16	5;16
206 073 023	sdB	BPS CS 29 512-38	15.00	3	3
210 837 690	sdB		15.11	4	4
212 498 842	sdB	EC 13 162-1229	15.26	6	6
212 465 180	sdB	EC 13 265-1313	15.56	6	6

Notes. T: engineering test from 4 to 13 February 2014; Campaign 0 (8 March–27 May 2014) to 18 (12 May–2 July 2018), https://keplergo.github.io/KeplerScienceWebsite/k2-fields.html

Table B.1. continued.

KIC	Class	Other name	Kp	Campaign (SC)	Campaign (LC)
212 160 066	sdB	SDSS J082445.68+231520.3	15.57	18	5;18
246 901 153	sdB	KUV 04369+1640	15.70	13	13
249 601 610	sdB	EC 15 050-2017	15.71	15	15
246 980 092	sdB	KUV 04482+1727	15.74	13	13
218 148 570	sdB		15.74	7	7
228 914 323	sdB	PG 1249-028	15.76	10 (101-102)	10 (101-102)
228 682 488	sdB	SDSS J085217.70+211637.4	16.00	16	16
212 818 294	sdB	PG 1356-047	16.15	6;17	6;17
248 422 838	sdB	PG 1032+007	16.27	14	14
214 515 136	sdB		16.30	7	7
251 603 936	sdB	SDSS J131916.15-011405.0	16.69	17	17
201 531 672	sdB	SDSS J112757.48+010044.2	16.89	1	1
251 457 058	sdB	SDSS J105428.85+010514.7	17.10	14	14
246 371 369	sdB	PB 5212	17.11	12	12
211 552 072	sdB	SDSS J084556.85+135211.3	17.50	16	16
212 567 176	sdB	HE 1309-1102	17.65	6	6
249 585 191	sdB	EC 15 064-2029	17.95	15	15
248 840 987	sdB	SDSS J102050.99+114024.3	18.15	14	14
248 810 568	sdOB	SDSS J110055.94+105542.3	14.22	14	14
246 997 679	sdOB	KUV 05109+1739	14.58	13	13
211 421 561	sdOB	SDSS J090042.68+115749.9	14.90	16	16
220 265 912	sdOB	PG 0055+016	15.19	8	8
249 700 050	sdOB	EC 15 059-1902	15.65	15	15
206 240 954	sdOB	SDSS J220337.88-090733.5	16.31	3	3
210 731 139	sdOB	SDSS J032427.24+184918.2	16.37	4	4
246 087 406	sdOB	PB 7470	16.46	12	12
206 186 190	sdOB	BPS CS 22 886-65	16.49	3	3
251 605 347	sdOB	SDSS J133611.02-011156.0	18.69	17	17
246 745 570	He-sdB	KUV 04456+1502	15.68	13	13
211 920 209	He-sdB	PG 0850+192	16.39	18	5; 16; 18
249 770 424	He-sdOB	GALEX J152332.2-181 726	14.00	15	15
211 495 446	He-sdOB	PG 0838+133	14.03	5;16	5;16
248 748 173	He-sdOB	PG 1033+097	16.38	14	14
248 761 152	He-sdOB	PG 1045+100	17.09	14	14
248 915 544	He-sdOB	SDSS J103806.64+134412.1	17.21	14	14
211 841 249	sdB	SDSSJ082734.96+175356.0	14.64	5;18	5;18
250 083 298	sdB	EC15203-1418	17.34	15	15
sdB/sdOB non pulsators, in binaries					
220 468 352	sdB+F	PB 6355	13.01	8	8
251 377 113	sdB+F/G	SDSS J090827.24+231417.9	13.53	16	16
211 499 370	sdB+F/G/K	SDSS J082556.80+130753.5	14.60	5	5;18
218 637 228	sdB+F/G		14.79	7	7
227 441 033	sdB+F/G		15.10	11 (111-112)	11 (111-112)
216 924 452	sdB+F/G		15.53	7	7
250 121 838	sdB+F/G/K	EC 15 365-1350	15.74	15	15
246 151 922	sdB+G9	HE 2322-0617	15.74	12;19	12;19
212 630 158	sdB+F/G		15.75	6	6
246 868 556	sdB+F/G	GALEX J050252.2+162647	15.78	13	13
246 864 591	sdB+F/G/K	KUV 04571+1620	15.98	13	13
211 910 684	sdB+F/G	PG 0906+191	15.99	16	16
212 108 396	sdB+F/G	SDSS J082447.30+221112.9	16.02	5	5;18
211 400 847	sdB+F/G	SDSS J084447.00+113910.0	16.43	5	5;18
212 003 762	sdB+F/G	SDSS J081406.79+201901.7	16.51	18	18
212 137 838	sdB+F/G	Ton 920	16.54	5	5
250 152 590	sdB+F/G/K	LB 889	17.13	15	15
248 467 942	sdB+F/G	SDSS J103022.07+020524.3	17.24	14	14
211 732 575	sdB+F/G	SDSS J082426.51+162145.1	17.68	18	18
251 583 165	sdB+F/G	SDSS J131932.19-014131.2	18.24	17	17
212 866 280	sdB+F/G	SDSS J133701.51-031732.2	18.27	17	17
212 410 755	sdB+WD	EC 13 332-1424	13.46	6	6
201 535 046	sdB+?	PG 1049+013	14.44	14	14
251 372 905	sdOB+F/G	SDSS J091216.06+225452.7	15.30	16	16
211 904 152	sdOB+F/G	PG 0912+189	15.93	16	16
248 767 552	sdOB+WD?	SDSS J101833.11+095336.1	14.97	14	14
246 877 984	sdOB+WD	KUV 05053+1628	16.11	13	13

Table B.1. continued.

KIC	Class	Other name	Kp	Campaign (SC)	Campaign (LC)
sdO non pulsators					
212 762 631	sdO	PG 1355-064	13.76	6	6;17
220 179 214	sdO	GD 934	14.93	8	8
248 520 995	sdO	SDSS J110053.55+034622.8	17.25	14	14
211 517 387	sdO	SDSS J082944.74+132302.5	17.32	5	5
249 862 817	sdO	EC 15 447-1656	18.05	15	15
228 821 386	He-sdO	PG 1220-056	14.86	10 (101-102)	10 (101-102)
249 867 379	He-sdO	EC 15 348-1652	15.35	15	15
205 247 324	He-sdO		16.01	2	2
201 640 895	He-sdO	SDSS J110215.45+024034.2	17.60	14	14
228 960 704	He-sdO	SDSS J123821.48-021211.4	18.49	10 (101-102)	10 (101-102)
Misc., in LC only					
201 150 341	sdB	HE 1140-0500	14.50	no data	1
214 958 569	sdB		15.70	no data	7
216 775 790	sdB		16.50	no data	7
201 236 182	sdB	PG 1154-031	16.59	no data	1
211 720 816	sdB	SDSS J083901.50+161148.0	16.71	no data	5; 16; 18
211 594 465	sdB	SDSS J081931.22+142756.1	17.19	no data	5; 18
248 912 731	sdB	SDSS J103832.41+133848.3	17.44	no data	14
201 201 339	sdB	SDSS J112757.48+010044.2	17.50	no data	1
201 590 024	sdB	SDSS J113418.00+015322.1	17.65	no data	1
201 698 091	sdB	SDSS J114821.29+033625.7	17.70	no data	1
229 021 782	sdB	SDSS J125410.86-010408.3	17.72	no data	10
228 682 339	sdB	SDSS J082824.20+212556.7	17.73	no data	5; 16; 18
251 457 060	sdB	SDSS J104725.10+010847.2	17.80	no data	14
248 783 069	sdB	SDSS J104620.14+101629.7	18.65	no data	14
251 410 019	sdB	SDSS J085809.09+252134.6	18.87	no data	16
201 424 163	sdB+WD	PG 1136-003	15.96	no data	1
228 682 347	sdB+WD	SDSS J083139.68+162316.4	17.91	no data	5
248 783 744	sdB+WD	SDSS J103218.40+101725.8	18.82	no data	14
211 460 944	sdB+WD ?	SDSS J084556.85+135211.3	15.36	no data	16
228 796 212	sdB	SDSS J124446.64-065625.8	18.83	no data	10
211 991 114	sd+F/G	Ton 914	15.10	no data	5; 18
211 930 840	He-sdB	SDSS J091512.06+191114.6	19.13	no data	16
201 734 164	sdOA	PG 1110+045	14.84	no data	1
213 545 287	sdOB	GALEX J191509.0-290 311	15.00	no data	7
201 924 421	sdOB	SDSS J113218.41+075103.0	17.20	no data	1
228 682 323	sdOB	SDSS J082110.89+183924.1	17.84	no data	5
212 034 957	sdOB	SDSS J090302.39+205008.9	18.62	no data	16
215 669 184	He-sdOB	GALEX J193323.6-234 553	15.00	no data	7
201 802 867	He-sdOB	SDSS J111633.29+052507.9	17.80	no data	1
251 383 153	He-sdOB	SDSS J091044.90+234044.6	18.27	no data	16
229 155 531	He-sdOB	SDSS J121643.72+020835.9	18.73	no data	10
251 357 585	He-sdOB	SDSS J092245.79+214238.9	19.01	no data	16
211 602 914	sd	SDSS J082959.28+143441.8	15.64	no data	5; 18
213 716 821	sdO	GALEX J192041.4-282 939	13.40	no data	7
246 735 349	He-sdO	KUV 04402+1455	13.97	no data	13
214 453 765	sdO	GALEX J191158.1-262 712	15.30	no data	7
216 452 306	He-sdO		16.40	no data	7
231 422 890	sdO		17.07	no data	11
201 418 759	sdO	SDSS J111438.57-004024.3	18.10	no data	1
201 843 731	sdO	SDSS J115009.48+061042.1	18.10	no data	1
211 559 083	sdO	SDSS J084421.10+135807.6	18.18	no data	16
228 682 365	He-sdO	SDSS J083747.23+194955.9	18.60	no data	5
216 747 137	sdO+dM	2MASS J18521800-2 147 506	13.87	no data	7
217 750 936	sdO+dM		16.70	no data	7

Appendix C: List of hot subdwarfs observed in the TESS primary mission

That is, Sector 1–26. The list is available at https://github.com/franpoz/Hot-Subdwarfs-Catalogues or at the CDS.

Appendix D: List of hot subdwarfs observed in the TESS extended mission

Sector 27–32. The list is available at https://github.com/franpoz/Hot-Subdwarfs-Catalogues or at the CDS.